Finite rotation meshfree formulation for geometrically nonlinear analysis of flat, curved and folded shells

S. Sadamoto[a,1], M. Ozdemir[b], S. Tanaka[a,*],
T.Q. Bui[c], S. Okazawa[d]

[a]*Graduate School of Engineering, Hiroshima University, Japan,*
e-mails: shota.sadamoto@gmail.com, satoyuki@hiroshima-u.ac.jp
[b]*Department of Naval Architecture and Marine Engineering,*
Ordu University, Turkey, e-mail:muratozdemir@odu.edu.tr
[c]*Department of Civil and Environmental Engineering,*
Tokyo Institute of Technology, Japan, e-mail:bui.t.aa@m.titech.ac.jp
[d]*Division of Mechanical Engineering, Faculty of Engineering,*
University of Yamanashi, Japan
e-mail:sokazawa@yamanashi.ac.jp

Abstract

Geometrically nonlinear analysis of flat, curved and folded shells under finite rotations is performed by enhanced six degrees of freedom (6-DOFs) meshfree formulation. Curvilinear surfaces are dealt with the concept of convected coordinates. Equilibrium equations are derived by total Lagrangian formulation with Green-Lagrange strain and Second Piola-Kirchhoff stress. Both shell geometry and its deformation are approximated by Reproducing Kernels (RKs). Transverse shear strains are considered by Mindlin-Reissner theory. Numerical integration of the stiffness matrix is estimated by using the Stabilized Conforming Nodal Integration (SCNI) method. To show accuracy and effectiveness of the proposed formulation and discretization, benchmark problems from the literatures are considered. Apart from reference solutions available in the literature, additional reference results based on finite element method (FEM) conducted by the present authors are also presented.

Keywords: meshfree methods, reproducing kernel, geometrically nonlinear analysis, finite rotation

---

[*] Corresponding author

[1] Current address: Fujitsu Limited, 9-3, Nakase 1-chome, Mihama-ku, Chiba city, Chiba 261-8588, Japan.

Preprint submitted to International Journal for Non-linear Mechanics October 7, 2019

---

1. Introduction

Nonlinear shell formulation is quite complex and requires special effort. Assumptions on the magnitude of deformations/rotations determine the limits of the theory in practice. Limited computer sources in the earlier times has restricted the computational works on the nonlinear shells, which in turn most of the works were conducted in analytical manner. Ref. [1] is one of the earlier analytical works on the nonlinear theory of thin shells assuming small mid-surface strains and moderate magnitude of rotations. Libai and Simmonds [2] applied large strain/rotations and material nonlinearities for the analysis of rings and shells. Stumpf [3] studied nonlinear buckling and post-buckling behavior of thin-shells assuming moderate rotations. Dvorkin and Bathe [4] developed four-node nonlinear shell element based on continuum mechanics, which may be assumed as one of pioneering works of the computational nonlinear shells. Then, the performance of that element type was examined by Stander *et al.* [5] by comparing with other assumed strain elements. Finite rotation thin-shell elements for the nonlinear analysis of doubly curved shells were developed by Başar and Ding [6]. Başar and his colleagues [7] then developed four-node and nine-node finite rotation shell elements by mixed formulation in which both displacements and force variables are interpolated. Previous finite rotation concepts were extended for composite shells refining shear deformation model by Başar *et al.* [8,9]. Recently, robust higher-order nonlinear shell formulations were proposed and various shell structures were analyzed [10-14].

In the aforementioned literature, the large deformation problems have been examined mainly by FEM. Beside this, Liu *et al.* [15] proposed Reproducing Kernel Particle Method (RKPM), and its applications for large deformations were formulated and demonstrated in Refs. [16,17]. Li *et al.* [18] proposed 3D RKPM formulation for the large deformation analysis of thin shell structures. Liew and his colleagues proposed RKPM formulation for the large deformation analysis of beams [19], then the RKPM concept was applied to nonlinear analysis of un-stiffened corrugated plates assuming small strains and first order shear deformation theory [20]. Zhao *et al.* [21] performed geometrically nonlinear analysis using the element-free kp-Ritz method for the cylindrical shells. SCNI [22,23] and Sub-domain Stabilized Conforming Integration (SSCI) [24-28] have been proposed for numerical integration techniques of the stiffness matrix. Wang and Sun [29,30] carried out geometrically nonlinear analyses of shear deformable beam and plates employing RKPM and SCNI. Peng *et al.* [31] proposed RKPM formulation for the geometrically nonlinear analysis on the basis of thick shell formulation.

Our research group performed geometrically nonlinear analysis employing meshfree methods [32-36]. Elastic large deflection analysis of plates with initial imperfections was carried out by the present authors employing convected coordinates [34,35]. Furthermore, geometrically nonlinear analysis of folded plate structures by 6-DOFs Galerkin meshfree formulation was conducted by Sadamoto *et al.* [36]. In the previous works of the authors, *i.e.*, [34-36], the rotation increments were assumed to be infinitesimal, and the finite rotation concept was not taken into account. In the present study, we extend previous geometrically nonlinear analysis concept for analyzing finite rotation problems.

The present work deals with the geometrically nonlinear analysis of flat, curved and folded shells assuming finite rotation increments in the convected coordinate system. Approximation of physical values and discretized geometry is conducted by means of RK functions, which are continuous in the support domain of the nodes. Plane stress condition is assumed for in-plane deformation while the Mindlin-Reissner shell formulation is adopted for transverse shear deformation. When evaluating the stiffness matrices, SCNI technique is employed for single geometries while both SCNI and SSCI are implemented for the numerical integration of plate assemblies along the connection of two plates. Essential boundary conditions (BCs) cannot be directly imposed due to lack of Kronecker Delta property in the meshfree interpolants. A boundary singular kernel (SK) [37] is thus employed to impose the so-called Kronecker Delta property in the set of the meshfree interpolants.

In the proposed method, continuous functions can be employed in the approximation for both in-plane and out-of-plane deformations; the discretization is relatively simple. The numerical discretization can be carried out in a straightforward manner. Treatment of shear locking problem, *e.g.*, reduced integration technique, is not needed. So far, meshfree shell formulations have been developed [31,38]; as far as the author's knowledge, the formulation including finite rotation problems are rather rare and the influence of finite rotation formulation was not specifically addressed, *e.g.*, see [31]. In the present work, the finite rotation problems are specifically selected and studied. A detailed comparison for with and without finite rotation cases is performed in terms of the convergence and the solution accuracy.

The rest of the paper is organized as follows. A shear-deformable shell formulation using a convected coordinate system as well as meshfree approximations are presented in Section 2. Finite rotation problem is addressed in Section 3. In Section 4, formulation for geometrically nonlinear analysis is described. Section 5 covers the numerical examples to demonstrate the capability of the present formulation for finite rotation problems utilizing flat, curved and folded structures. Main conclusions are drawn in Section 6.

2. Shell kinematics and meshfree approximations

2.1. Shell kinematics

A shell model as illustrated in Fig. 1 with the reference coordinates is considered. In the given figure, $\boldsymbol{X}$=(X_1, X_2, X_3) is a position vector in the Cartesian coordinate system, while $\boldsymbol{r}$=(r_1, r_2, r_3) stands for a position vector in the convected coordinates. The unit base vectors are expressed as $\boldsymbol{e}_i$ $(i = 1, 2, 3)$ along the $\boldsymbol{X}_i$ axes, respectively. The coordinate transformation between Cartesian and convected coordinate system is carried out by a special technique, which is similar to that of Noguchi *et al.* [39] in order to effectively deal with the curvilinear surfaces. By this technique, any arbitrary shape of shell surface can be transformed and represented in the corresponding convected coordinates, and vice-versa.

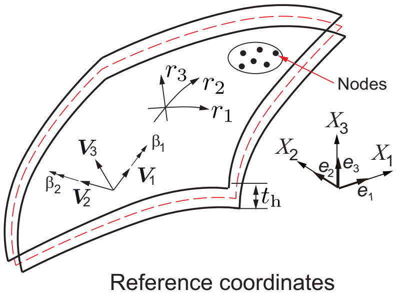

Figure 1: A schematic illustration of a shell model with reference coordinates.

The shell is assumed to have a uniform thickness t_h throughout the analysis domain. Moderately thin and thick shell assumptions are made in the present formulation based on Mindlin-Reissner theory. The material is assumed to be homogeneous isotropic and elastic.

Initial position, $\boldsymbol{X}$, and the position at time t, ${}^t\boldsymbol{x}$, of a point on a shell surface can be given by

$$\boldsymbol{X} = \boldsymbol{X}_{\mathrm{mid}} + \frac{r_3}{2} t_{\mathrm{h}} {}^0\boldsymbol{V}_3, \tag{1}$$

$${}^t\boldsymbol{x} = {}^t\boldsymbol{x}_{\mathrm{mid}} + \frac{r_3}{2} t_{\mathrm{h}} {}^t\boldsymbol{V}_3. \tag{2}$$

Here, $\boldsymbol{X}_{\mathrm{mid}}$ and ${}^t\boldsymbol{x}_{\mathrm{mid}}$ are the coordinates of the mid-thickness plane of the shell in the Cartesian coordinate system. The directors at the initial and current configuration are denoted as ${}^0\boldsymbol{V}_3$ and ${}^t\boldsymbol{V}_3$, respectively. Denoting the time increment $\Delta t = t' - t$, the displacement increment of a point, $\boldsymbol{u}$ for the given time increment Δt is expressed as:

$$\boldsymbol{u} = {}^{t'}\boldsymbol{x} - {}^t\boldsymbol{x} = {}^{t'}\boldsymbol{u}_{\mathrm{mid}} - {}^t\boldsymbol{u}_{\mathrm{mid}} + \frac{r_3}{2} t_{\mathrm{h}} ({}^{t'}\boldsymbol{V}_3 - {}^t\boldsymbol{V}_3). \tag{3}$$

The displacement can also be written in terms of orthogonal unit vectors ${}^t\boldsymbol{V}_1$ and ${}^t\boldsymbol{V}_2$ on the mid-thickness plane and rotation components β_1 and β_2 as:

$$\boldsymbol{u} = \boldsymbol{u}_{\mathrm{mid}} + \frac{r_3}{2} t_{\mathrm{h}} (-\beta_1 {}^t\boldsymbol{V}_2 + \beta_2 {}^t\boldsymbol{V}_1). \tag{4}$$

The displacement vector in Eq. (4) can be written explicitly as:

$$\boldsymbol{u} = \begin{Bmatrix} u_1 \\ u_2 \\ u_3 \end{Bmatrix} = \begin{Bmatrix} u_{\mathrm{mid1}} - \frac{r_3}{2} t_{\mathrm{h}} \beta_1 {}^t\boldsymbol{V}_{2(1)} + \frac{r_3}{2} t_{\mathrm{h}} \beta_2 {}^t\boldsymbol{V}_{1(1)} \\ u_{\mathrm{mid2}} - \frac{r_3}{2} t_{\mathrm{h}} \beta_1 {}^t\boldsymbol{V}_{2(2)} + \frac{r_3}{2} t_{\mathrm{h}} \beta_2 {}^t\boldsymbol{V}_{1(2)} \\ u_{\mathrm{mid3}} - \frac{r_3}{2} t_{\mathrm{h}} \beta_1 {}^t\boldsymbol{V}_{2(3)} + \frac{r_3}{2} t_{\mathrm{h}} \beta_2 {}^t\boldsymbol{V}_{1(3)} \end{Bmatrix}. \tag{5}$$

In Eq. (5), $\boldsymbol{V}_{i(j)}$ terms represent the dot products of the unit vectors $\boldsymbol{V}_i$ and $\boldsymbol{e}_j$.

2.2. Approximation of curved shells and its deformations by RKs

Shear deformable shell modeling based on RKs and SCNI can prevent shear locking phenomenon by imposing Kirchhoff mode reproducing condition [40,41] and it was analyzed in Ref. [34] for flat shells and employed for fracture mechanics analysis [42,43]. The meshfree interpolant is utilized for the curved shell. They are distributed on the convected coordinate system as shown in Fig. 1 and it can be written for the I-th node as:

$$\psi_I(r_1, r_2) = \boldsymbol{h}^T(r_{1I} - r_1, r_{2I} - r_2)\boldsymbol{b}(r_1, r_2)\phi_I(r_{1I} - r_1, r_{2I} - r_2). \tag{6}$$

$\boldsymbol{b}(r_1, r_2)$ is a coefficient vector. A complete quadratic basis $\boldsymbol{h}(r_{1I} - r_1, r_{2I} - r_2)(= \{1 \;\; r_1 \;\; r_2 \;\; r_1^2 \;\; r_1 r_2 \;\; r_2^2\})$ is employed. A cubic spline function is taken as an original kernel function $\phi_I(r_{1I} - r_1, r_{2I} - r_2)$, as:

$$\phi_I = \frac{10}{7\pi h_I^2} \begin{cases} 1 - \frac{3}{2}s_I^2 + \frac{3}{4}s_I^3 & (0 \leq s_I \leq 1) \\ \frac{1}{4}(2 - s_I)^3 & (1 \leq s_I \leq 2) \\ 0 & (2 \leq s_I) \end{cases} . \tag{7}$$

$s_I(=\sqrt{(r_{1I} - r_1)^2 + (r_{2I} - r_2)^2}/h_I)$ is the normalized distance from center of the kernel and h_I is a parameter to define the function support. The function support of the RKs set as 2.4 to 2.7 of a characteristic length between the I-th node and neighboring nodes.

In the meshfree Galerkin discretization of the curved shells, the RK functions are employed not only for the curved geometry interpolation, but also for the field variables approximation. The approximation scheme is conceptually same with the isoparametric FEM. The completeness condition can thus be met. Nodes can be randomly distributed on the mid-thickness plane as shown in Fig. 1 and the orthogonal unit vector $\boldsymbol{V}_i$ is defined at each node; *i.e.*, $\boldsymbol{V}_{iI}$ for the I-th node. A position vector $\boldsymbol{X}_{\text{mid}}(r_1, r_2)$ on the mid-thickness plane (r_1-r_2 plane) of the curved shell is interpolated using the RKs as:

$$\boldsymbol{X}_{\text{mid}}(r_1, r_2) = \sum_{I=1}^{\text{NP}} \psi_I(r_1, r_2) \boldsymbol{X}_{\text{mid}I}, \tag{8}$$

$$\boldsymbol{X}(r_1, r_2) = \sum_{I=1}^{\text{NP}} \psi_I(r_1, r_2) \left(\boldsymbol{X}_{\text{mid}I} + \frac{r_3}{2} t_{\text{h}}{}^0 \boldsymbol{V}_{3I} \right), \tag{9}$$

where $\psi_I(r_1, r_2)$ and $\boldsymbol{X}_{\text{mid}I}$ are the interpolation function and position vector of the I-th node on the mid-thickness plane, respectively. NP is the total number of scattered nodes used for the interpolation of the mid-thickness plane of the curved shell. As for the details of RKs, see Ref. [44]. As similar to approximation of the position vector, the displacement vector on mid-thickness plane can be approximated as:

$$\boldsymbol{u}_{\text{mid}}(\boldsymbol{r}) = \sum_{I=1}^{\text{NP}} \psi_I(\boldsymbol{r}) \boldsymbol{u}_{\text{mid}I}, \quad \boldsymbol{u}(\boldsymbol{r}) = \sum_{I=1}^{\text{NP}} \psi_I(\boldsymbol{r}) \left(\boldsymbol{u}_{\text{mid}I} + \frac{r_3}{2} t_{\text{h}}{}^0 \boldsymbol{V}_{3I} \right). \tag{10}$$

The displacement increment $\boldsymbol{u}$ is expressed as follows using RK functions:

$$\boldsymbol{u} = \left\{ \begin{array}{c} u_1 \\ u_2 \\ u_3 \end{array} \right\} = \sum_{I=1}^{\mathrm{NP}} \left[\begin{array}{ccccc} \psi_I & 0 & 0 & -\frac{t_{\mathrm{h}}}{2} r_3 \psi_I {}^t\boldsymbol{V}_{2(1)} & \frac{t_{\mathrm{h}}}{2} r_3 \psi_I {}^t\boldsymbol{V}_{1(1)} \\ 0 & \psi_I & 0 & -\frac{t_{\mathrm{h}}}{2} r_3 \psi_I {}^t\boldsymbol{V}_{2(2)} & \frac{t_{\mathrm{h}}}{2} r_3 \psi_I {}^t\boldsymbol{V}_{1(2)} \\ 0 & 0 & \psi_I & -\frac{t_{\mathrm{h}}}{2} r_3 \psi_I {}^t\boldsymbol{V}_{2(3)} & \frac{t_{\mathrm{h}}}{2} r_3 \psi_I {}^t\boldsymbol{V}_{1(3)} \end{array} \right] \left\{ \begin{array}{c} u_{1I} \\ u_{2I} \\ u_{3I} \\ \beta_{1I} \\ \beta_{2I} \end{array} \right\}$$

$$= \sum_{I=1}^{\mathrm{NP}} \boldsymbol{\Psi}_I \boldsymbol{U}_I. \tag{11}$$

Here, u_{iI} (i=1,2,3) are displacement increments in the mid-thickness plane, while β_{1I} and β_{2I} are the rotation components for the I-th node with respect to r_1 and r_2-axes, respectively.

In case of geometrically nonlinear problems, the local orthogonal basis vectors have to be updated for each incremental step. Then, the orthogonal basis vectors can be approximated by RK functions as:

$${}^t\boldsymbol{V}_i(r_1, r_2) = \sum_{I=1}^{\mathrm{NP}} \psi_I(r_1, r_2) {}^t\boldsymbol{V}_{iI}, \quad (i = 1, 2, 3). \tag{12}$$

The covariant base vectors $\boldsymbol{G}_i$ have to be introduced to map between the Cartesian and the convected coordinates. This can be achieved through the following relations:

$$\boldsymbol{G}_i = \frac{\partial \boldsymbol{X}}{\partial r_i} = \sum_{I=1}^{\mathrm{NP}} \frac{\partial \psi_I(r_1, r_2)}{\partial r_i} \left(\boldsymbol{X}_I + \frac{r_3}{2} t_{\mathrm{h}} {}^0\boldsymbol{V}_{3I} \right), \quad (i = 1, 2), \tag{13}$$

$$\boldsymbol{G}_3 = \frac{\partial \boldsymbol{X}}{\partial r_3} = \sum_{I=1}^{\mathrm{NP}} \psi_I(r_1, r_2) \frac{1}{2} t_{\mathrm{h}} {}^0\boldsymbol{V}_{3I}. \tag{14}$$

The covariant base vector, ${}^t\boldsymbol{g}_i$, at time t is expressed in terms of covariant base vector at initial configuration and displacement vector as:

$${}^t\boldsymbol{g}_i = \frac{\partial \boldsymbol{x}}{\partial r_i} = \frac{\partial (\boldsymbol{X} + {}^t\boldsymbol{u})}{\partial r_i} = \boldsymbol{G}_i + \frac{\partial {}^t\boldsymbol{u}}{\partial r_i}. \tag{15}$$

2.3. Rotation components and rotation angles

In order to derive 6-DOFs formulation, the relationship between the rotation angles and rotation components is introduced here, see Fig. 2(a). First, it is assumed that the rotation is small for each increment. In the given figure, the drilling rotation component, β_3 and the drilling rotation angle, θ_3 are defined. Implementation of a drilling rotation component has already been presented in our previous studies [45-47]. Then, the displacement approximations are modified considering these relations. The rotation of director, ω is schematically illustrated in Fig. 2(b).

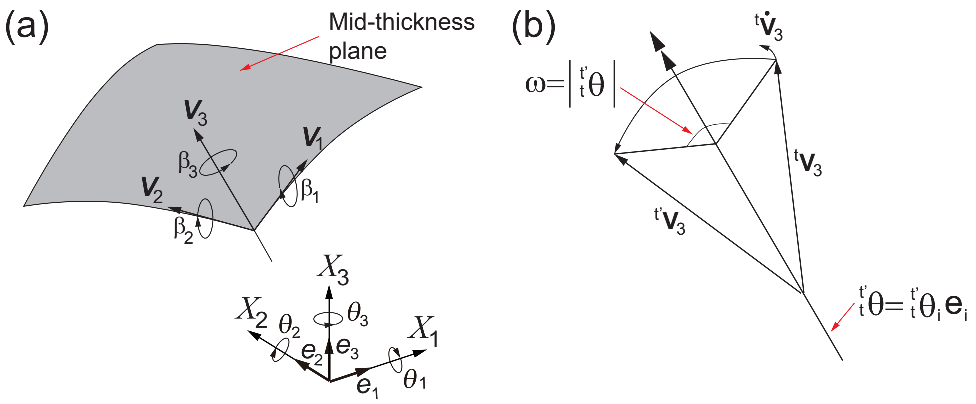

Figure 2: Rotation of directors: (a) rotation components β_i and angles θ_i, (b) orthogonal transformation of shell director, $\boldsymbol{V}_3$.

The rotation vector of directors, $\boldsymbol{\omega}$ is expressed considering rotation angles, rotation components and unit vectors as:

$$\boldsymbol{\omega} = \beta_i \boldsymbol{V}_i = \theta_j \boldsymbol{e}_j. \tag{16}$$

The rotation components then can be written as:

$$\beta_i = \boldsymbol{V}_i \cdot \boldsymbol{e}_j \theta_j = \boldsymbol{V}_{i(j)} \theta_j. \tag{17}$$

The relationship is written in explicit form as follows:

$$\left\{ \begin{array}{c} \beta_1 \\ \beta_2 \\ \beta_3 \end{array} \right\} = \left[\begin{array}{ccc} \boldsymbol{V}_{1(1)} & \boldsymbol{V}_{1(2)} & \boldsymbol{V}_{1(3)} \\ \boldsymbol{V}_{2(1)} & \boldsymbol{V}_{2(2)} & \boldsymbol{V}_{2(3)} \\ \boldsymbol{V}_{3(1)} & \boldsymbol{V}_{3(2)} & \boldsymbol{V}_{3(3)} \end{array} \right] \left\{ \begin{array}{c} \theta_1 \\ \theta_2 \\ \theta_3 \end{array} \right\}. \tag{18}$$

Then, the kinematic relations for small rotations can be rewritten considering Eq. (18) as:

$$\boldsymbol{u}_{\mathrm{s}} = \boldsymbol{u}_{\mathrm{mid}} + \frac{r_3}{2} t_{\mathrm{h}} (-(\boldsymbol{\theta} \cdot {}^{t}\boldsymbol{V}_1) {}^{t}\boldsymbol{V}_2 + (\boldsymbol{\theta} \cdot {}^{t}\boldsymbol{V}_2) {}^{t}\boldsymbol{V}_1), \tag{19}$$

where $\boldsymbol{V}_i$=$\{\boldsymbol{V}_{i(1)}\ \boldsymbol{V}_{i(2)}\ \boldsymbol{V}_{i(3)}\}$ and $\boldsymbol{\theta}$=$\{\theta_1\ \theta_2\ \theta_3\}^T$. $\boldsymbol{u}_{\mathrm{s}}$ is a displacement vector for small rotation. The derivatives of the displacement vector are given as:

$$\begin{aligned}\frac{\partial \boldsymbol{u}_{\mathrm{s}}}{\partial r_i} =& \frac{\partial \boldsymbol{u}_{\mathrm{mid}}}{\partial r_i} + \frac{r_3}{2} t_{\mathrm{h}} \Bigg(-\frac{\partial}{\partial r_i} (\boldsymbol{\theta} \cdot {}^t\boldsymbol{V}_1)^t\boldsymbol{V}_2 - (\boldsymbol{\theta} \cdot {}^t\boldsymbol{V}_1) \frac{\partial^t \boldsymbol{V}_2}{\partial r_i} \\ & + \frac{\partial}{\partial r_i} (\boldsymbol{\theta} \cdot {}^t\boldsymbol{V}_2)^t\boldsymbol{V}_1 + (\boldsymbol{\theta} \cdot {}^t\boldsymbol{V}_2) \frac{\partial^t \boldsymbol{V}_1}{\partial r_i} \Bigg) \ (i = 1,\ 2), \end{aligned} \tag{20}$$

$$\frac{\partial \boldsymbol{u}_{\mathrm{s}}}{\partial r_3} = \frac{1}{2} t_{\mathrm{h}} (-(\boldsymbol{\theta} \cdot {}^t\boldsymbol{V}_1)^t\boldsymbol{V}_2 + \big(\boldsymbol{\theta} \cdot {}^t\boldsymbol{V}_2)^t\boldsymbol{V}_1\big) \, . \tag{21}$$

Then, the displacement vector and derivatives can be approximated by RKs in convected coordinates as:

$$\begin{aligned}\boldsymbol{u}_{\mathrm{s}} &= \sum_{I=1}^{\mathrm{NP}} \begin{bmatrix} \psi_I & 0 & 0 & r_3\boldsymbol{A}'_{1(1)} & r_3\boldsymbol{A}'_{2(1)} & r_3\boldsymbol{A}'_{3(1)} \\ 0 & \psi_I & 0 & r_3\boldsymbol{A}'_{1(2)} & r_3\boldsymbol{A}'_{2(2)} & r_3\boldsymbol{A}'_{3(2)} \\ 0 & 0 & \psi_I & r_3\boldsymbol{A}'_{1(3)} & r_3\boldsymbol{A}'_{2(3)} & r_3\boldsymbol{A}'_{3(3)} \end{bmatrix} \begin{Bmatrix} u_{1I} \\ u_{2I} \\ u_{3I} \\ \theta_{1I} \\ \theta_{2I} \\ \theta_{3I} \end{Bmatrix} \\ &= \sum_{I=1}^{\mathrm{NP}} \boldsymbol{\Psi}_I \boldsymbol{W}_I, \end{aligned} \tag{22}$$

$$\begin{aligned}\frac{\partial \boldsymbol{u}_{\mathrm{s}}}{\partial r_i} &= \sum_{I=1}^{\mathrm{NP}} \begin{bmatrix} \frac{\partial \psi_I}{\partial r_i} & 0 & 0 & r_3\boldsymbol{A}''_{i1(1)} & r_3\boldsymbol{A}''_{i2(1)} & r_3\boldsymbol{A}''_{i3(1)} \\ 0 & \frac{\partial \psi_I}{\partial r_i} & 0 & r_3\boldsymbol{A}''_{i1(2)} & r_3\boldsymbol{A}''_{i2(2)} & r_3\boldsymbol{A}''_{i3(2)} \\ 0 & 0 & \frac{\partial \psi_I}{\partial r_i} & r_3\boldsymbol{A}''_{i1(3)} & r_3\boldsymbol{A}''_{i2(3)} & r_3\boldsymbol{A}''_{i3(3)} \end{bmatrix} \boldsymbol{W}_I \\ &= \sum_{I=1}^{\mathrm{NP}} \boldsymbol{\Psi}_{I,i} \boldsymbol{W}_I, \ (i = 1, 2), \end{aligned} \tag{23}$$

$$\begin{aligned}\frac{\partial \boldsymbol{u}_{\mathrm{s}}}{\partial r_3} &= \sum_{I=1}^{\mathrm{NP}} \begin{bmatrix} 0 & 0 & 0 & \boldsymbol{A}'_{1(1)} & \boldsymbol{A}'_{2(1)} & \boldsymbol{A}'_{3(1)} \\ 0 & 0 & 0 & \boldsymbol{A}'_{1(2)} & \boldsymbol{A}'_{2(2)} & \boldsymbol{A}'_{3(2)} \\ 0 & 0 & 0 & \boldsymbol{A}'_{1(3)} & \boldsymbol{A}'_{2(3)} & \boldsymbol{A}'_{3(3)} \end{bmatrix} \boldsymbol{W}_I \\ &= \sum_{I=1}^{\mathrm{NP}} \boldsymbol{\Psi}_{I,3} \boldsymbol{W}_I, \end{aligned} \tag{24}$$

where θ_{iI} (i=1, 2, 3) are rotation angles of I-th node. $\boldsymbol{A}'_i$ and $\boldsymbol{A}''_{ij}$ are expressed as:

$$\boldsymbol{A}'_i = \frac{t_\mathrm{h}}{2}\psi_I \left({}^t\boldsymbol{V}_{2(i)}{}^t\boldsymbol{V}_1 - {}^t\boldsymbol{V}_{1(i)}{}^t\boldsymbol{V}_2\right), \tag{25}$$

and

$$\begin{aligned}\boldsymbol{A}''_{ij} = \frac{t_\mathrm{h}}{2}\Bigg[\psi_I \left({}^t\boldsymbol{V}_{2(j)}\frac{\partial^t\boldsymbol{V}_1}{\partial r_i} + \frac{\partial^t\boldsymbol{V}_{2(j)}}{\partial r_i}{}^t\boldsymbol{V}_1 - {}^t\boldsymbol{V}_{1(j)}\frac{\partial^t\boldsymbol{V}_2}{\partial r_i} - \frac{\partial^t\boldsymbol{V}_{1(j)}}{\partial r_i}{}^t\boldsymbol{V}_2\right) \\ + \frac{\partial\psi_I}{\partial r_i}({}^t\boldsymbol{V}_{2(j)}{}^t\boldsymbol{V}_1 - {}^t\boldsymbol{V}_{1(j)}{}^t\boldsymbol{V}_2)\Bigg].\end{aligned} \tag{26}$$

A penalty formulation proposed by Kanok-Nukulchai [48] is employed to introduce drilling rotation component based on convected coordinate system into a virtual work equation. A mid-thickness is assumed β_1-β_2 plane as shown in Fig. (2) and a penalty energy Q_T is defined as:

$$Q_T = \kappa_T \int_V C^{1212}\left[\beta_3|\boldsymbol{G}_1\times\boldsymbol{G}_2| - \frac{1}{2}\left(\boldsymbol{G}_2\cdot\frac{\partial\boldsymbol{u}}{\partial r_1} - \boldsymbol{G}_1\cdot\frac{\partial\boldsymbol{u}}{\partial r_2}\right)\right]^2 dV. \tag{27}$$

κ_T is a coefficient of the penalty energy and utilized as κ_T=0.1. C^{1212} is a shear term in the elastic constitutive tensor. β_3 is the virtual in-plane rotation. The virtual distortion ε_{β_3} and the corresponding virtual stress R_{β_3} caused by β_3 is respectively given as:

$$\varepsilon_{\beta_3} = \left[\beta_3|\boldsymbol{G}_1\times\boldsymbol{G}_2| - \frac{1}{2}\left(\boldsymbol{G}_2\cdot\frac{\partial\boldsymbol{u}}{\partial r_1} - \boldsymbol{G}_1\cdot\frac{\partial\boldsymbol{u}}{\partial r_2}\right)\right]\boldsymbol{G}_1\otimes\boldsymbol{G}_2, \tag{28}$$

$$R_{\beta_3} = 2\kappa_T\, C^{1212}\varepsilon_{\beta_3}\boldsymbol{G}^1\otimes\boldsymbol{G}^2. \tag{29}$$

3. Introduction of finite rotation

So far, the formulation is derived assuming the rotation increment is infinitesimal. As long as the rotation increment and the total rotation are small and they are precisely updated, the given formulation is basically accurate. On the other hand, even if the load/rotation increment is small, this formulation has a limitation on the total magnitude of the rotations [49].

In general, there are two ways, Euler angle and rotation of axial vector, to introduce finite rotation into FEM formulation [50]. Surana [49] and Stander *et al.* [5] implemented Euler angle for degenerated shell elements. In the application of Euler angles as the primary kinematic variables, some problems occur when the rotation angle gets larger than 90°. This problem was discussed by Parisch [51] based on the references therein.

Argyris [52] has proposed finite rotation formulation by introducing axial vector to the nonlinear formulation by means of rotation of director. In the formulation, update of the rotation angle is carried out by multiplying rotation tensor with the director of the shell. Noguchi and Hisada [50,53,54] implemented finite rotation tensor into FEM assuming the axial vector is constant during each load increment. They employed Taylor series expansion and the first two terms are utilized. Using this formulation, the singularity of the stiffness matrix caused by the finite rotation terms can be avoided. Our finite rotation formulation is based on the approach given by Noguchi and Hisada [50,53,54] whose procedure is described below.

Finite rotation tensor ${}^{t'}_{t}\boldsymbol{R}$ is defined to account for the finite rotation increment. As for the rotation up to time t' of the director ${}^{t}\boldsymbol{V}_3$ of the shell, it is assumed that the rotation axis does not change during rotation. Orthogonal transformation of the director is schematically illustrated in Fig. 2(b). ${}^{t'}_{t}\boldsymbol{\theta}$ is the axis of rotation, and ω is the finite rotation angle. At this time:

$$ {}^{t'}_{t}\boldsymbol{\theta} = {}^{t'}_{t}\theta_i \boldsymbol{e}_i, \tag{30}$$

$$ \omega = |{}^{t'}_{t}\boldsymbol{\theta}|. \tag{31}$$

The antisymmetric matrix ${}^{t'}_{t}\boldsymbol{\Phi}$ is defined using the components of the axial vector ${}^{t'}_{t}\boldsymbol{\theta}$.

$$ {}^{t'}_{t}\boldsymbol{\Phi} = \left[\begin{array}{ccc} 0 & -{}^{t'}_{t}\theta_3 & {}^{t'}_{t}\theta_2 \\ {}^{t'}_{t}\theta_3 & 0 & -{}^{t'}_{t}\theta_1 \\ -{}^{t'}_{t}\theta_2 & {}^{t'}_{t}\theta_1 & 0 \end{array} \right]. \tag{32}$$

Dividing Eqs. (30) and (32) by Δt, spin tensor and its axial vector can be obtained as follow in case of small rotation problem.

$$ {}^{t'}_{t}\boldsymbol{\Phi}{}^{t}\boldsymbol{V}_3 = {}^{t'}_{t}\boldsymbol{\theta} \times {}^{t}\boldsymbol{V}_3 = {}^{t}\dot{\boldsymbol{V}}_3, \tag{33}$$

where $(\ \dot{}\ )$ represents an increment quantity. From the expression in Eq. (33), $\boldsymbol{I} + 1/n {}^{t'}_{t}\boldsymbol{\Phi}$ makes a small rotation tensor between $\Delta t/n$ with ω/n. The finite rotation can therefore be considered as a set of infinitesimal rotation. From this fact, the finite rotation tensor ${}^{t'}_{t}\boldsymbol{R}$ can be defined as follows:

$$
\begin{aligned}
{}^{t'}_{t}\boldsymbol{R} &= \lim_{n\to\inf}\left(\boldsymbol{I}+\frac{1}{n}{}^{t'}_{t}\boldsymbol{\Phi}\right)^{n} \\
&= \boldsymbol{I}+{}^{t'}_{t}\boldsymbol{\Phi}+\frac{1}{2!}\left({}^{t'}_{t}\boldsymbol{\Phi}\right)^{2}+\frac{1}{3!}\left({}^{t'}_{t}\boldsymbol{\Phi}\right)^{3}+\cdots . \qquad (34)
\end{aligned}
$$

In the derivation of the tangential stiffness, it is sufficient to consider only the first and second terms of the right-hand side in Eq. (34). Then, the finite rotation tensor can be practically expressed as:

$$
{}^{t'}_{t}\boldsymbol{R} = \boldsymbol{I}+{}^{t'}_{t}\boldsymbol{\Phi}+\frac{1}{2}\left({}^{t'}_{t}\boldsymbol{\Phi}\right)^{2}. \qquad (35)
$$

On the other hand, the exact rotation tensor ${}^{t'}_{t}\boldsymbol{R}$ is obtained from the geometric relationship according to Argyris [52]. It is written as:

$$
{}^{t'}_{t}\boldsymbol{R} = \boldsymbol{I}+\frac{\sin\omega}{\omega}{}^{t'}_{t}\boldsymbol{\Phi}+\frac{1}{2}\left(\frac{\sin(\omega/2)}{\omega/2}\right)^{2}\left({}^{t'}_{t}\boldsymbol{\Phi}\right)^{2}. \qquad (36)
$$

Considering the finite rotational increment, the displacement increment is expressed as:

$$
\begin{aligned}
\boldsymbol{u} &= \boldsymbol{u}_{\mathrm{mid}}+\frac{r_3}{2}t_{\mathrm{h}}({}^{t'}_{t}\boldsymbol{R}-\boldsymbol{I})\,{}^{t}\boldsymbol{V}_3 \\
&= \boldsymbol{u}_{\mathrm{mid}}+\frac{r_3}{2}t_{\mathrm{h}}\,{}^{t'}_{t}\boldsymbol{\theta}\times{}^{t}\boldsymbol{V}_3+\frac{r_3}{2}t_{\mathrm{h}}\,{}^{t'}_{t}\boldsymbol{\theta}\times({}^{t'}_{t}\boldsymbol{\theta}\times{}^{t}\boldsymbol{V}_3) \\
&= \left(\boldsymbol{u}_{\mathrm{mid}}+\frac{r_3}{2}t_{\mathrm{h}}\,(-\beta_1{}^{t}\boldsymbol{V}_2+\beta_2{}^{t}\boldsymbol{V}_1)\right)+\left(-\frac{r_3}{4}t_{\mathrm{h}}\,(\beta_1^2+\beta_2^2){}^{t}\boldsymbol{V}_3\right) \\
&= \boldsymbol{u}_{\mathrm{s}}+\boldsymbol{u}_{\mathrm{ex}}. \qquad (37)
\end{aligned}
$$

Here $\boldsymbol{u}_{\mathrm{s}}$ denotes the displacement increment in case of small rotation shown so far, and $\boldsymbol{u}_{\mathrm{ex}}$ is additional term associated with the finite rotation increment.

The partial derivatives of the displacement increment with respect to convected coordinates can be expressed as:

$$
\begin{aligned}
\frac{\partial\boldsymbol{u}}{\partial r_i} &= \frac{\partial\boldsymbol{u}_{\mathrm{s}}}{\partial r_i}-\frac{r_3}{2}t_{\mathrm{h}}\left(\beta_1\frac{\partial\beta_1}{\partial r_i}+\beta_2\frac{\partial\beta_2}{\partial r_i}\right){}^{t}\boldsymbol{V}_3-\frac{r_3}{4}t_{\mathrm{h}}(\beta_1^2+\beta_2^2)\frac{\partial{}^{t}\boldsymbol{V}_3}{\partial r_i} \\
&= \frac{\partial\boldsymbol{u}_{\mathrm{s}}}{\partial r_i}+\frac{\partial\boldsymbol{u}_{\mathrm{ex}}}{\partial r_i},\quad (i=1,2), \qquad (38)
\end{aligned}
$$

$$
\frac{\partial\boldsymbol{u}}{\partial r_3} = \frac{\partial\boldsymbol{u}_{\mathrm{s}}}{\partial r_3}-\frac{1}{4}t_{\mathrm{h}}\,(\beta_1^2+\beta_2^2){}^{t}\boldsymbol{V}_3 = \frac{\partial\boldsymbol{u}_{\mathrm{s}}}{\partial r_3}+\frac{\partial\boldsymbol{u}_{\mathrm{ex}}}{\partial r_3}. \qquad (39)
$$

The material derivatives of the strain increments and the variation can be written as:

$$ {}_{t_0}\dot{E}_{\mathrm{L}ij} = \frac{1}{2}\left({}^{t}\boldsymbol{g}_i \cdot \frac{\partial \dot{\boldsymbol{u}}_{\mathrm{s}}}{\partial r_j} + {}^{t}\boldsymbol{g}_j \cdot \frac{\partial \dot{\boldsymbol{u}}_{\mathrm{s}}}{\partial r_i} \right), \tag{40} $$

$$ \delta_{t_0} E_{\mathrm{L}ij} = \frac{1}{2}\left({}^{t}\boldsymbol{g}_i \cdot \frac{\partial \delta \boldsymbol{u}_{\mathrm{s}}}{\partial r_j} + {}^{t}\boldsymbol{g}_j \cdot \frac{\partial \delta \boldsymbol{u}_{\mathrm{s}}}{\partial r_i} \right), \tag{41} $$

$$ \begin{aligned} (\delta_{t_0} E_{\mathrm{NL}ij})^{\cdot} = {} & \frac{1}{2}\left(\frac{\partial \dot{\boldsymbol{u}}_{\mathrm{s}}}{\partial r_i} \cdot \frac{\partial \delta \boldsymbol{u}_{\mathrm{s}}}{\partial r_j} + \frac{\partial \delta \boldsymbol{u}_{\mathrm{s}}}{\partial r_i} \cdot \frac{\partial \dot{\boldsymbol{u}}_{\mathrm{s}}}{\partial r_j} \right) \\ & + \frac{1}{2}\left({}^{t}\boldsymbol{g}_i \cdot \frac{\partial (\delta \boldsymbol{u}_{\mathrm{ex}})^{\cdot}}{\partial r_j} + {}^{t}\boldsymbol{g}_j \cdot \frac{\partial (\delta \boldsymbol{u}_{\mathrm{ex}})^{\cdot}}{\partial r_i} \right). \end{aligned} \tag{42} $$

They are utilized in the virtual work equation. It is only necessary to add the second term of the Eq. (42) to the geometric stiffness matrix. In computing the convergence of the residual force, the director is updated using the exact finite rotation tensor, which is shown in Eq. (36), to obtain the strain increments.

4. Geometrically nonlinear analysis

4.1. Total Lagrangian method

Total Lagrangian formulation with Green-Lagrange strain and Second Piola-Kirchhoff stress is adopted for representing large deflections and rotations. The virtual work equation for the unknown state of deformation $t'{=}t+\Delta t$ can be expressed in terms of Green-Lagrange strain tensor ${}^{t}_{t_0}\boldsymbol{E}$ and Second Piola-Kirchhoff stress tensor ${}^{t}_{t_0}\boldsymbol{S}$ as:

$$ \int_V {}^{t'}_{0}\boldsymbol{S} : \delta\, {}^{t'}_{0}\boldsymbol{E} dV = {}^{t'}\delta R. \tag{43} $$

The suffixes on the lower left side of the stress and strain tensors denote the reference configuration. In Eq. (43), $t_0{=}0$ that is the initial configuration. On the other hand, ${}^{t'}\delta R$ is the virtual work term associated with external forces. V stands for the volume of the initial configuration. Green-Lagrange strain tensor can be decomposed by the covariant base vectors for the current t and unknown configuration t' as follows.

$$ {}^{t}_{0}\boldsymbol{E} = \frac{1}{2}\left({}^{t}\boldsymbol{g}_i \cdot {}^{t}\boldsymbol{g}_j - \boldsymbol{G}_i \cdot \boldsymbol{G}_j \right) \boldsymbol{G}^i \otimes \boldsymbol{G}^j, \tag{44} $$

$$ {}^{t'}_{0}\boldsymbol{E} = \frac{1}{2}\left({}^{t'}\boldsymbol{g}_i \cdot {}^{t'}\boldsymbol{g}_j - \boldsymbol{G}_i \cdot \boldsymbol{G}_j \right) \boldsymbol{G}^i \otimes \boldsymbol{G}^j. \tag{45} $$

Then, Green-Lagrange strain increment can be expressed by

$$\begin{aligned}{}_{0}\boldsymbol{E} = {}^{t'}_{0}\boldsymbol{E} - {}^{t}_{0}\boldsymbol{E} &= {}_{0}E_{ij}\boldsymbol{G}^{i} \otimes \boldsymbol{G}^{j} \\ &= \frac{1}{2}\left({}^{t'}\boldsymbol{g}_{i} \cdot {}^{t'}\boldsymbol{g}_{j} - {}^{t}\boldsymbol{g}_{i} \cdot {}^{t}\boldsymbol{g}_{j}\right)\boldsymbol{G}^{i} \otimes \boldsymbol{G}^{j}. \end{aligned} \tag{46}$$

As for the Second Piola-Kirchhoff stress tensor for the unknown configuration, decomposition is carried out as:

$${}^{t'}_{0}\boldsymbol{S} = {}^{t}_{0}\boldsymbol{S} + {}_{0}\boldsymbol{S} = \left({}^{t}_{0}S^{ij} + {}_{0}S^{ij}\right)\boldsymbol{G}_{i} \otimes \boldsymbol{G}_{j}. \tag{47}$$

Finally, the virtual work equation in Eq. (43) is decomposed as follow.

$$\begin{aligned}\int_{V} {}_{0}S^{ij}\left(\delta_{0}E_{\mathrm{L}ij} + \delta_{0}E_{\mathrm{NL}ij}\right)dV &+ \int_{V} {}^{t}_{0}S^{ij}\delta_{0}E_{\mathrm{NL}ij}dV \\ &= {}^{t'}\delta R - \int_{V} {}^{t}_{0}S^{ij}\delta_{0}E_{\mathrm{L}ij}dV. \end{aligned} \tag{48}$$

Left hand side of Eq. (48) is nonlinear in terms of the displacement increment $\boldsymbol{u}$. Thus, linearization has to be performed. Applying the linearization, stress velocity and strain rate concepts come out, and the relationship between the stress velocity and strain rate can be given by

$${}^{t}_{0}\dot{\boldsymbol{S}} = {}_{0}\bar{\boldsymbol{C}} : {}^{t}_{0}\dot{\boldsymbol{E}}, \tag{49}$$

where the dot over the stress and strain increments denote the linearized terms divided by the $\Delta t \to 0$. ${}_{0}\bar{\boldsymbol{C}}$ is the constituent tensor.

An elastic material is assumed. The constitutive equation is given employing $\boldsymbol{V}_{i}$, as:

$${}_{0}\bar{\boldsymbol{C}} = {}_{0}\bar{C}_{ijkl}\boldsymbol{V}_{i} \otimes \boldsymbol{V}_{j} \otimes \boldsymbol{V}_{k} \otimes \boldsymbol{V}_{l}. \tag{50}$$

The matrix ${}_{0}\bar{C}_{ijkl}$ is written as:

$$\begin{aligned}{}_{0}\bar{\boldsymbol{C}} &= \begin{bmatrix} {}_{0}\bar{C}_{1111} & {}_{0}\bar{C}_{1122} & {}_{0}\bar{C}_{1112} & {}_{0}\bar{C}_{1123} & {}_{0}\bar{C}_{1131} \\ {}_{0}\bar{C}_{2211} & {}_{0}\bar{C}_{2222} & {}_{0}\bar{C}_{2212} & {}_{0}\bar{C}_{2223} & {}_{0}\bar{C}_{2231} \\ {}_{0}\bar{C}_{1211} & {}_{0}\bar{C}_{1222} & {}_{0}\bar{C}_{1212} & {}_{0}\bar{C}_{1223} & {}_{0}\bar{C}_{1231} \\ {}_{0}\bar{C}_{2311} & {}_{0}\bar{C}_{2322} & {}_{0}\bar{C}_{2312} & {}_{0}\bar{C}_{2323} & {}_{0}\bar{C}_{2331} \\ {}_{0}\bar{C}_{3111} & {}_{0}\bar{C}_{3122} & {}_{0}\bar{C}_{3112} & {}_{0}\bar{C}_{3123} & {}_{0}\bar{C}_{3131} \end{bmatrix} \\ &= \frac{E}{1-\nu^{2}}\begin{bmatrix} 1 & \nu & & & \\ & 1 & & 0 & \\ & & \frac{1-\nu}{2} & & \\ & \text{sym.} & & \kappa\frac{1-\nu}{2} & \\ & & & & \kappa\frac{1-\nu}{2} \end{bmatrix}, \end{aligned} \tag{51}$$

where E, ν and κ are Young's modulus, Poisson's ratio and shear modulus, respectively. It can be expressed as a contradiction component using covariant base vectors $\boldsymbol{G}_i$ as:

$$ {}_0\bar{\boldsymbol{C}} = {}_0\bar{C}^{ijkl}\boldsymbol{G}_i \otimes \boldsymbol{G}_j \otimes \boldsymbol{G}_k \otimes \boldsymbol{G}_l. \tag{52} $$

They have following relation as:

$$ {}_0\bar{C}^{ijkl} = {}_0\bar{C}_{mnop}(\boldsymbol{V}_m \cdot \boldsymbol{G}^i)(\boldsymbol{V}_n \cdot \boldsymbol{G}^j)(\boldsymbol{V}_o \cdot \boldsymbol{G}^k)(\boldsymbol{V}_p \cdot \boldsymbol{G}^l). \tag{53} $$

And the relationship between associated stress and strain tensors is:

$$ {}^t_0\dot{S}^{ij} = {}_0\bar{C}^{ijkl}\,{}^t_0\dot{E}_{\mathrm{L}kl}. \tag{54} $$

As for drilling rotation component, a virtual energy δQ_T due to virtual strain $\delta\varepsilon_{\beta_3}$ is proposed in Eq. (55). Employing incremental decomposition and linearization, virtual energy can be expressed as:

$$ \left(\frac{1}{2}\int_V t_0\dot{R}_{\beta_3}\delta_0\varepsilon_{\beta_3}dV\right)\Delta t = -\frac{1}{2}\int_V {}_0R_{\beta_3}\delta_0\varepsilon_{\beta_3}dV. \tag{55} $$

Finally, the virtual work equation can be written as:

$$ \begin{aligned} &\left(\int_V {}_0\bar{C}^{ijkl}\,{}_0\dot{E}_{kl}\delta_0E_{\mathrm{L}ij}dV + \int_V {}^t_0S^{ij}(\delta_0E_{\mathrm{NL}ij})^{\cdot}dV + \int_V \kappa_T\,{}_0C^{1212}\,{}_0\dot{\varepsilon}_{\beta_3}\delta_0\varepsilon_{\beta_3}dV\right)\Delta t \\ &\qquad = {}^{t'}\delta R - \int_V {}^t_0S^{ij}\delta_0E_{\mathrm{L}ij}dV - \frac{1}{2}\int_V {}^t_0R_{\beta_3}\delta_0\varepsilon_{\beta_3}dV. \end{aligned} \tag{56} $$

4.2. Discretization

Discretization of the virtual work equation is presented. ${}_0\dot{E}_{ij}$ in first term of left hand side of Eq. (56) can be represented in vector form as:

$$ {}_0\hat{\dot{\boldsymbol{E}}} = \left\{ \begin{array}{c} {}_0\dot{E}_{11} \\ {}_0\dot{E}_{22} \\ 2{}_0\dot{E}_{12} \\ 2{}_0\dot{E}_{23} \\ 2{}_0\dot{E}_{31} \end{array} \right\} = \left[\begin{array}{c} {}^t\boldsymbol{g}_1 \cdot \frac{\partial \dot{\boldsymbol{u}}}{\partial r^1} \\ {}^t\boldsymbol{g}_2 \cdot \frac{\partial \dot{\boldsymbol{u}}}{\partial r^2} \\ {}^t\boldsymbol{g}_1 \cdot \frac{\partial \dot{\boldsymbol{u}}}{\partial r^2} + {}^t\boldsymbol{g}_2 \cdot \frac{\partial \dot{\boldsymbol{u}}}{\partial r^1} \\ {}^t\boldsymbol{g}_2 \cdot \frac{\partial \dot{\boldsymbol{u}}}{\partial r^3} + {}^t\boldsymbol{g}_3 \cdot \frac{\partial \dot{\boldsymbol{u}}}{\partial r^2} \\ {}^t\boldsymbol{g}_3 \cdot \frac{\partial \dot{\boldsymbol{u}}}{\partial r^1} + {}^t\boldsymbol{g}_1 \cdot \frac{\partial \dot{\boldsymbol{u}}}{\partial r^3} \end{array} \right]. \tag{57} $$

The partial derivatives of $\dot{\boldsymbol{u}}$ on the convected coordinate system $\partial\dot{\boldsymbol{u}}/\partial r_i$ are discretized by RKs as given in Eqs. (23) and (24). It is given in matrix form as:

$$
\begin{aligned}
{}_0\dot{\hat{\boldsymbol{E}}} &= \sum_{I=1}^{\mathrm{NP}} \begin{bmatrix} {}^t\boldsymbol{g}_1^T\boldsymbol{\Psi}_{I,1} \\ {}^t\boldsymbol{g}_2^T\boldsymbol{\Psi}_{I,2} \\ {}^t\boldsymbol{g}_1^T\boldsymbol{\Psi}_{I,2} + {}^t\boldsymbol{g}_2^T\boldsymbol{\Psi}_{I,1} \\ {}^t\boldsymbol{g}_2^T\boldsymbol{\Psi}_{I,3} + {}^t\boldsymbol{g}_3^T\boldsymbol{\Psi}_{I,2} \\ {}^t\boldsymbol{g}_3^T\boldsymbol{\Psi}_{I,1} + {}^t\boldsymbol{g}_1^T\boldsymbol{\Psi}_{I,3} \end{bmatrix} \dot{\boldsymbol{W}}_I \\
&= \sum_{I=1}^{\mathrm{NP}} {}^t_0\boldsymbol{B}_{\mathrm{L}I}\dot{\boldsymbol{W}}_I,
\end{aligned}
\tag{58}
$$

where ${}^t_0\boldsymbol{B}_{\mathrm{L}I}$ is a matrix of displacement-strain relationship. In the similar manner, $\delta_0 E_{\mathrm{L}ij}$ in Eq. (56) is written in vector form as:

$$
\delta_0\hat{\boldsymbol{E}}_{\mathrm{L}} = \sum_{I=1}^{\mathrm{NP}} {}^t_0\boldsymbol{B}_{\mathrm{L}I}\delta\boldsymbol{W}_I,
\tag{59}
$$

where $\delta\boldsymbol{W}_I$ is a variation of $\boldsymbol{W}_I$. Therefore, first term of Eq. (56) is discretized as:

$$
\begin{aligned}
\left(\int_V {}_0\bar{C}^{ijkl}\,{}_0\dot{E}_{kl}\,\delta_0 E_{\mathrm{L}ij}\,dV\right)\Delta t =& \delta\boldsymbol{W}^T\int_V {}^t_0\boldsymbol{B}_{\mathrm{L}}^T\,{}_0\bar{\boldsymbol{C}}\;{}^t_0\boldsymbol{B}_{\mathrm{L}}\,dV\;\boldsymbol{W}, \\
=& \delta\boldsymbol{W}^T\,{}^t_0\boldsymbol{K}_L\boldsymbol{W}.
\end{aligned}
\tag{60}
$$

where $\boldsymbol{W}^T$=$\{\boldsymbol{W}_1,\cdots,\boldsymbol{W}_{\mathrm{NP}}\}^T$ and ${}^t_0\boldsymbol{B}_{\mathrm{L}}$=$[{}^t_0\boldsymbol{B}_{\mathrm{L}1},\ \cdots,\ {}^t_0\boldsymbol{B}_{\mathrm{LNP}}]$. ${}^t_0\boldsymbol{K}_L$ is a initial displacement matrix. The volume of the shell is defined by vector triple product as: dV=$[{}^0\boldsymbol{g}_1\,{}^0\boldsymbol{g}_2\,{}^0\boldsymbol{g}_3]dr^1dr^2dr^3$. The matrix of elastic constitutive model is given in Eq. (51).

Additionally, second term of left hand side in Eq. (56) is discretized. The term includes variation of displacement increment and material derivative. Here, we define a vector $\dot{\boldsymbol{d}}$ as:

$$
\dot{\boldsymbol{d}}^T = \left\{\ \left(\frac{\partial\dot{\boldsymbol{u}}}{\partial r_1}\right)^T\ \ \left(\frac{\partial\dot{\boldsymbol{u}}}{\partial r_2}\right)^T\ \ \left(\frac{\partial\dot{\boldsymbol{u}}}{\partial r_3}\right)^T\ \right\}.
\tag{61}
$$

The increment of partial derivatives $\partial\dot{\boldsymbol{u}}/\partial r_i$ are derived by Eqs. (23) and (24) taking the finite rotation term in Eqs. (38) and (39) into account. The following relation can be obtained as:

$$\dot{\boldsymbol{d}} = \sum_{I=1}^{\mathrm{NP}} \begin{bmatrix} \boldsymbol{\Psi}_{I,1} \\ \boldsymbol{\Psi}_{I,2} \\ \boldsymbol{\Psi}_{I,3} \end{bmatrix} \dot{\boldsymbol{W}}_I = \sum_{I=1}^{\mathrm{NP}} {}^t_0\boldsymbol{B}_{\mathrm{NL}I} \dot{\boldsymbol{W}}_I. \tag{62}$$

In a similar manner, the variation component can also be discretized. Finally, the second term of left hand side of Eq. (56) is written as:

$$\begin{aligned} \left(\int_V {}^t_0S^{ij} (\delta_0 E_{\mathrm{NL}ij})^{\cdot}\, dV \right) \Delta t =& \delta \boldsymbol{W}^T \int_V {}^t_0\boldsymbol{B}^T_{\mathrm{NL}} {}^t_0\bar{\boldsymbol{S}}\, {}^t_0\boldsymbol{B}_{\mathrm{NL}} dV\ \boldsymbol{W}, \\ =& \delta \boldsymbol{W}^T \{ {}^t_0\boldsymbol{K}_{\mathrm{NLs}} + {}^t_0\boldsymbol{K}_{\mathrm{NLex}} \} \boldsymbol{W}, \end{aligned} \tag{63}$$

where ${}^t_0\boldsymbol{B}_{\mathrm{NL}}$=$[{}^t_0\boldsymbol{B}_{\mathrm{NL1}}, \ \cdots\ , \ {}^t_0\boldsymbol{B}_{\mathrm{NLNP}}]$. ${}^t_0\boldsymbol{K}_{\mathrm{NLs}}$ is an initial stiffness matrix and ${}^t_0\boldsymbol{K}_{\mathrm{NLex}}$ is additional term in terms of finite rotation components. ${}^t_0\bar{\boldsymbol{S}}$ is a matrix in terms of Second Piola-Kirchhoff stress. It is presented in matrix form as:

$${}^t_0\bar{\boldsymbol{S}} = \begin{bmatrix} {}^t_0S^{11}\boldsymbol{I} & {}^t_0S^{12}\boldsymbol{I} & {}^t_0S^{13}\boldsymbol{I} \\ {}^t_0S^{21}\boldsymbol{I} & {}^t_0S^{22}\boldsymbol{I} & {}^t_0S^{23}\boldsymbol{I} \\ {}^t_0S^{31}\boldsymbol{I} & {}^t_0S^{32}\boldsymbol{I} & \boldsymbol{0} \end{bmatrix}, \tag{64}$$

where $\boldsymbol{I}$ is 3×3 unit matrix.

Second term of right hand side in Eq. (56) is discretized by employing displacement-strain matrix ${}^t_0\boldsymbol{B}_{\mathrm{L}}$ in Eq. (60). It is derived as:

$$\begin{aligned} \int_V {}^t_0S^{ij} \delta_0 E_{\mathrm{L}ij} dV =& \delta \boldsymbol{W}^T \int_V {}^t_0\boldsymbol{B}^T_{\mathrm{L}} {}^t_0\hat{\boldsymbol{S}} dV \\ =& \delta \boldsymbol{W}^T {}^t_0\boldsymbol{Q}, \end{aligned} \tag{65}$$

where ${}^t_0\boldsymbol{Q}$ is an internal force vector. ${}^t_0\hat{\boldsymbol{S}}$ is a vector defined as:

$${}^t_0\hat{\boldsymbol{S}}^T = \left\{ \ {}^t_0S^{11} \quad {}^t_0S^{22} \quad {}^t_0S^{12} \quad {}^t_0S^{23} \quad {}^t_0S^{31} \ \right\}. \tag{66}$$

Based on above discretization, following linear equation is evaluated.

$$\left({}^t_0\boldsymbol{K}_{\mathrm{L}} + {}^t_0\boldsymbol{K}_{\mathrm{NL}} \right) \boldsymbol{W} = {}^{t'}\boldsymbol{F} - {}^t_0\boldsymbol{Q}. \tag{67}$$

${}^{t'}\boldsymbol{F}$ is a vector in terms of external force ${}^{t'}\delta R$. ${}^t_0\boldsymbol{K}_{\mathrm{NL}}$= $({}^t_0\boldsymbol{K}_{\mathrm{NLs}} + {}^t_0\boldsymbol{K}_{\mathrm{NLex}})$ is initial stiffness matrix including finite rotation term. The equation is then solved by Newton-Raphson method.

4.3. Nodal integration

In order to conduct numerical integration of the matrices in Eq. (67), SCNI [22,23] is employed. A flat shell model is arranged and nodes are distributed on the flat shell model. Voronoi cells are generated to define the volume and for the nodal integration. And then, a curved shell geometry is constructed through the convected coordinate system. For simplicity, the components $u_{\mathrm{mid}1}$, $u_{\mathrm{mid}2}$, $u_{\mathrm{mid}3}$, θ_1, θ_2 and θ_3 are rewritten as u_i (i=1, $\cdots$, 6).

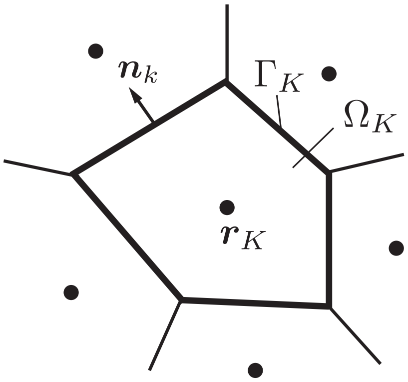

Figure 3: Nodal integration with SCNI.

The domain form of the partial derivatives $u_{j,k}(\boldsymbol{r})$ is transformed to the line integration with Gauss' divergence theorem. The physical quantities are smoothed within the entire cell. When adopting SCNI for K-th node $\boldsymbol{r}_K$ in Fig. 3(b), it is written as:

$$\begin{aligned} \tilde{u}^h_{j,k}(\boldsymbol{r}_K) &= \frac{1}{A_K}\int_{\Omega_K} u^h_{j,k}(\boldsymbol{r})\; d\Omega \\ &= \frac{1}{A_K}\int_{\Gamma_K} u^h_j(\boldsymbol{r}) n_k \; d\Gamma = \sum_{I=1}^{\mathrm{NP}} b_{Ik}(\boldsymbol{r}_K) u_{jI}, \\ b_{Ik}(\boldsymbol{r}_K) &= \frac{1}{A_K}\int_{\Gamma_K} \psi_I(\boldsymbol{r}) n_k \; d\Gamma, \quad j=\{1,\cdots,6\}, \quad k=\{1,2\}, \end{aligned} \tag{68}$$

where ($\tilde{\ }$) stands for smoothed values. Ω_K and Γ_K are domain and boundary of Voronoi cell for K-th node. A_K is area of Ω_K. n_k is normal to the boundary Γ_K.

SSCI [24-28] is only applied for connection of folded structure in the numerical examples to accurately integrate the tangent stiffness matrix.

5. Numerical examples and discussion

The accuracy and effectiveness of the present meshfree formulation with finite rotation are examined by conducting large displacement/rotation analysis of shell structures assuming elastic material properties. The influence of finite rotation formulation is investigated in terms of the solution accuracy as well as the convergence. The convergence term for each load increment is evaluated and compared with the assumed order of convergence, 10^{-5}. The convergence term is the ratio of residual forces norm to the external forces norm.

Numerical examples are selected among the well-known benchmark problems of the geometrically nonlinear analysis as well as the finite rotation problems available in the literature. As a first example, we consider one of most popular benchmark problems, pinched cylinder under a point load. Then, a simple geometry that is a clamped rectangular plate problem with a tip moment is considered. As the third numerical example, a complex geometry that is a trapezoidal plate problem under an end moment is studied. Finally, roll up of L-shaped plate problem is analyzed under tip moment. In both problems, shells are subjected to large displacement/rotations and membrane locking must be addressed. Meshfree results are compared with the reference papers as well as FEM based results obtained by the present authors.

For the FEM computations, ANSYS [56] software is employed adopting Shell181 shell elements. Shell181 element formulation is based on bi-linear shape functions and Mindlin-Reissner shear deformation theory [56]. This element is suitable for simulating large displacement/rotation problems.

5.1. Pinched cylinder under point load

The pinched cylinder problem is not a specific finite rotation problem but it is a well-known numerical example for geometrically nonlinear analysis. This problem was numerically examined by many papers *e.g.*, [57-59] and references therein. Owing to its curvilinear surface, this numerical example should be a good verification of the present method for the geometrically nonlinear analysis using the convected coordinates. The pinched cylinder problem is depicted in Fig. 4.

The dimensions and material properties are same as Ref. [57]. The cylinder length, radius and thickness are L=3.048, R=1.016 and t_{h}=0.03, respectively. The material properties are E=2.0685 $\times$ 10^7 and ν=0.3.

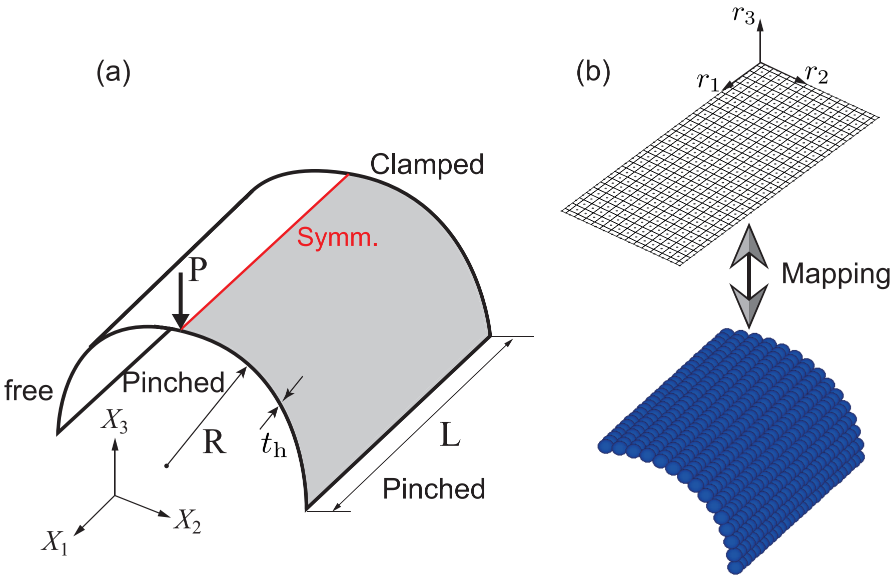

Figure 4: Modeling of the pinched cylinder: (a) representative model with symmetric BCs, (b) meshfree modeling using mapping technique.

The maximum load, P_{max} is 2,000. Moreover, not only graphical but also numerical tabulated results are provided in Ref. [58]. Half cylinder FEM model as similar to [58] with 32×32 elements is adopted. For the meshfree computations, a quarter model with 435 nodes and symmetric BCs as given in Fig. 4 is developed. It must be noted that when the quarter model is considered, the applied maximum load is taken as half of P_{max}.

The meshfree results obtained by the present formulation are compared with the FEM based results obtained by the authors and tabulated results given by Ref. [58] in Fig. 5. In the figure, the vertical displacement of load application point is plotted with respect to the load increment. The results obtained by the proposed method are represented by “MFree”. It is evident that a very good agreement is achieved between the results.

The vertical displacement of the load application point at the end of loading computed by the present finite rotation formulation is 1.712, while the FEM result computed by the authors and reference result given by Ref. [58] are 1.719 and 1.715, respectively. The relative error for the vertical displacement based on Ref. [58] then becomes 0.175 %.

Even though, the pinched cylinder is not a specific finite rotation problem;

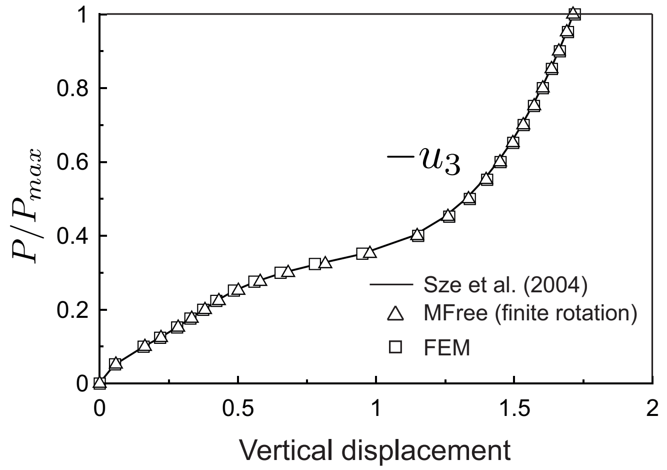

Figure 5: Vertical displacement of the load application point.

we can examine the influence of finite rotation formulation on the results regarding the convergence. The vertical displacements of the load application point with and without finite rotation formulation cases are almost the same, which is difficult to distinguish in a graph. We therefore check the average number of convergence iterations for each load increment. Average number of convergence iterations for each load increment is 2.1 when finite rotation formulation is considered. On the other hand, the average number of convergence iterations for each load increment becomes 10.0 when the finite rotation formulation is out of consideration. Such a big difference in the number of convergence iterations notably influences the computational efficiency. The deformed shapes evaluated by FEM and present meshfree computations are illustrated in Fig. 6. The figure indicates the good agreement between the FEM and meshfree models.

Finite rotation computation is carried out for non-uniform nodal distributions. The meshfree model in Fig. 4(b) is employed and the nodal coordinates are re-arranged by introducing a parameter for irregular distribution as follow.

$$\boldsymbol{x}_{\text{irr}} = \boldsymbol{x} + (2.0\ r_c - 1.0) \cdot \Delta s \cdot \gamma_{\text{irr}}, \tag{69}$$

where $\boldsymbol{x}$ and $\boldsymbol{x}_{\text{irr}}$ are the position vectors of a node for regular and irregular arrangement. Δs is a characteristic length between the target node and

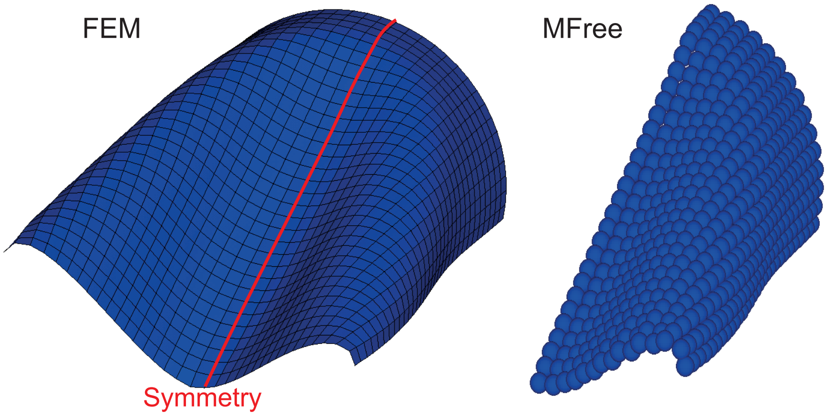

Figure 6: Deformed shapes for pinched cylinder at $P/P_{max} = 1$.

neighboring nodes. r_c is a random number, and γ_{irr} is an irregularity factor. γ_{irr}=0.2, 0.3 and 0.4 are chosen. The meshfree models are shown in Fig. 7(a)-(c) for γ_{irr}=0.2, 0.3 and 0.4, respectively.

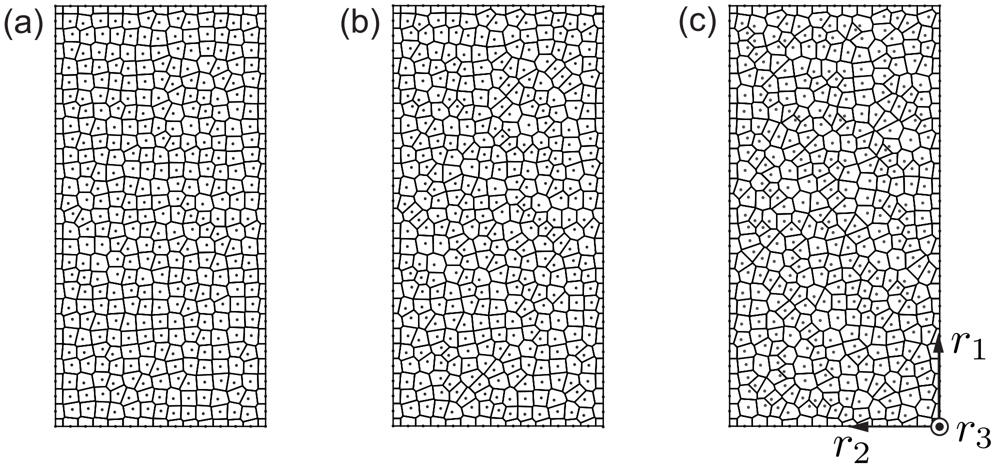

Figure 7: Non-uniform meshfree models: (a) γ_{irr}=0.2, (b) γ_{irr}=0.3, (c) γ_{irr}=0.4.

The meshfree results are shown in Fig. 8. Although the convergence for each load increment gradually worsens as γ_{irr} is increased, the problem can be analyzed by non-uniform meshfree models with good accuracy.

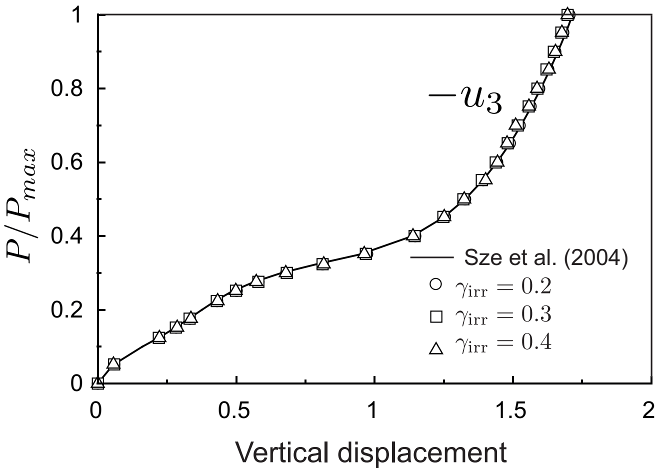

Figure 8: Vertical displacement of the load application point for the non-uniform meshfree models.

5.2. Roll up of a rectangular plate

One of popular benchmark studies for the finite rotation problems, a cantilever rectangular plate subjected to tip moment is considered. This problem was addressed in Refs. [31,58] as well as the references therein. A schematic illustration with main properties is given in Fig. 9. Under the tip moment, the cantilever plate forms a circular arc shape with the radius, $R{=}EI/M$, where I stands for the second moment of area for vertical bending. Normalized deflections can be analytically calculated by [58].

$$\frac{U}{L} = \frac{M_0}{M} \sin\left(\frac{M}{M_0}\right), \tag{70}$$

$$\frac{W}{L} = \frac{M_0}{M} \left(1 - \cos\left(\frac{M}{M_0}\right)\right), \tag{71}$$

where $M_0{=}EI/L$. The maximum tip moment, $M_{\rm max}{=}2\pi M_0$, at which the cantilever plate forms a circle.

The roll up of a rectangular plate is a specific finite rotation problem so that the finite rotation terms must be taken into account to get the solution up to maximum moment. In the meshfree computations, there must be enough number of nodes within the support domain of RK functions.

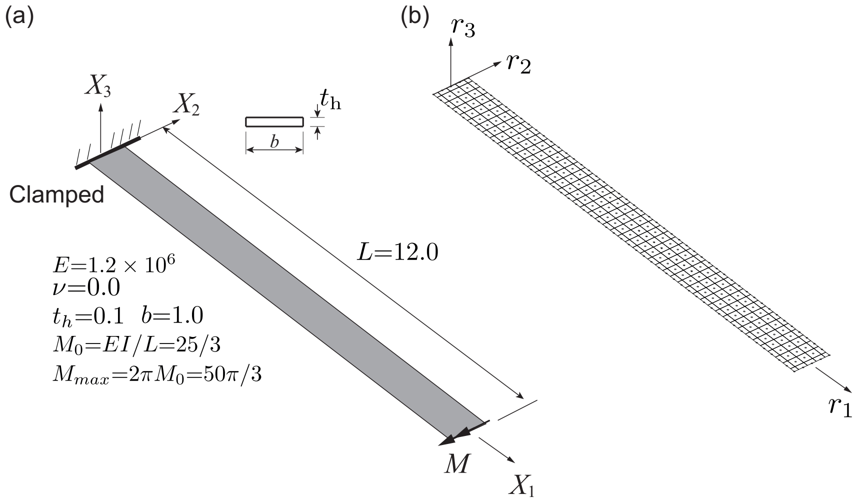

Figure 9: Cantilever rectangular plate model: (a) representative model and main properties, (b) meshfree model with Voronoi cells.

Considering this condition, five nodes are allocated along r_2-direction. To keep the nodal distance same in the whole body, 49 nodes are utilized in r_1-direction. In this case, the nodal distance becomes $b/4$ within the whole body and the total number nodes for the meshfree model is 245.

Comparison of present meshfree formulation including finite rotation terms and analytical results obtained through Eqs. (70) and (71) are given in Fig. 10, which clearly indicates that the proposed method with finite rotation formulation has capability of dealing with large rotation problems precisely. Analytical value of the tip rotation is 360°, while the tip rotation by the proposed method is 359.7°; error for the tip rotation then becomes 0.075 %.

The FEM results are compared with present formulation considering with and without finite rotation cases in Fig. 11. It is evident from the figure that the proposed method with finite rotation formulation correlates very well with the FEM results, while neglecting the finite rotation terms leads poor estimation of the tip displacement. In addition, the meshfree method without finite rotation terms fails to converge before reaching the maximum moment. Moreover, average number of the convergence iterations for each load increment becomes 33.6 when the finite rotation formulation is neglected, while average number of the convergence iterations for each load increment is obtained as 2.2 in case of the finite rotation terms are considered. These

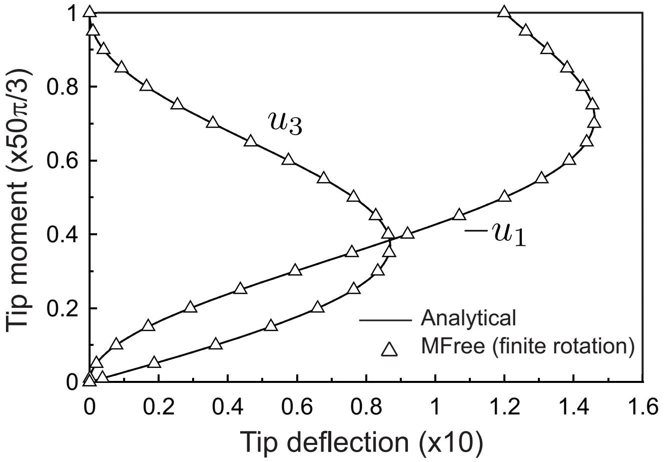

Figure 10: Comparison of meshfree results with the analytical solutions by Eqs. (70) and (71).

values apparently indicate the influence of finite rotation formulation on the computational efficiency.

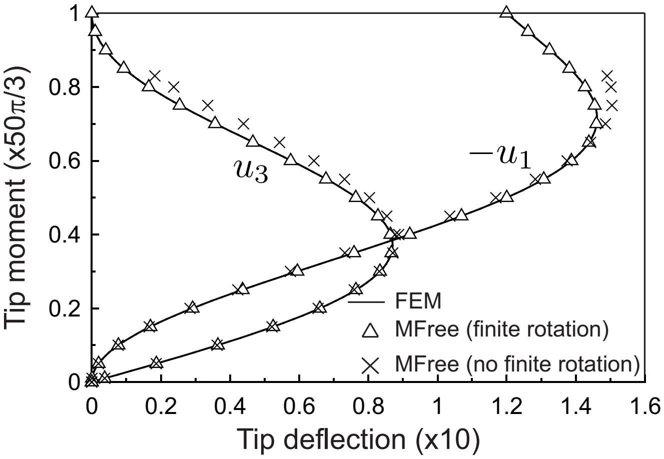

Figure 11: Influence of finite rotation terms on the tip displacements of rectangular plate.

Finally, the deformed shapes are given in Fig. 12 for FEM and meshfree formulation with and without finite rotation terms. Deformed shapes obtained by FEM and proposed method with finite rotation formulation are in good agreement, while the meshfree results without finite rotation formulation fails to converge and maximum moment value cannot be reached.

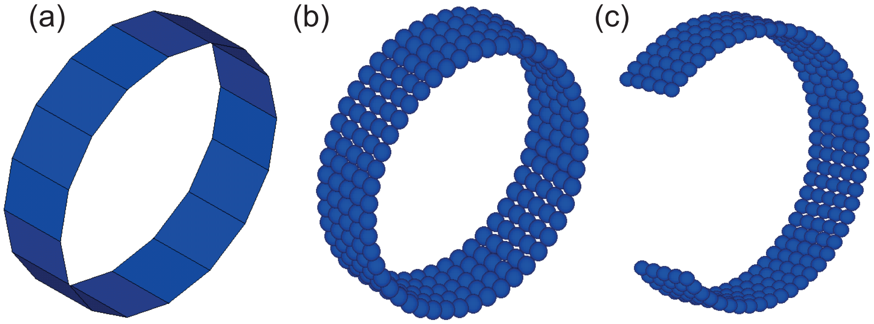

Figure 12: Deformed shapes for rectangular plate: (a) FEM, (b) MFree (finite rotation), (c) MFree (without finite rotation).

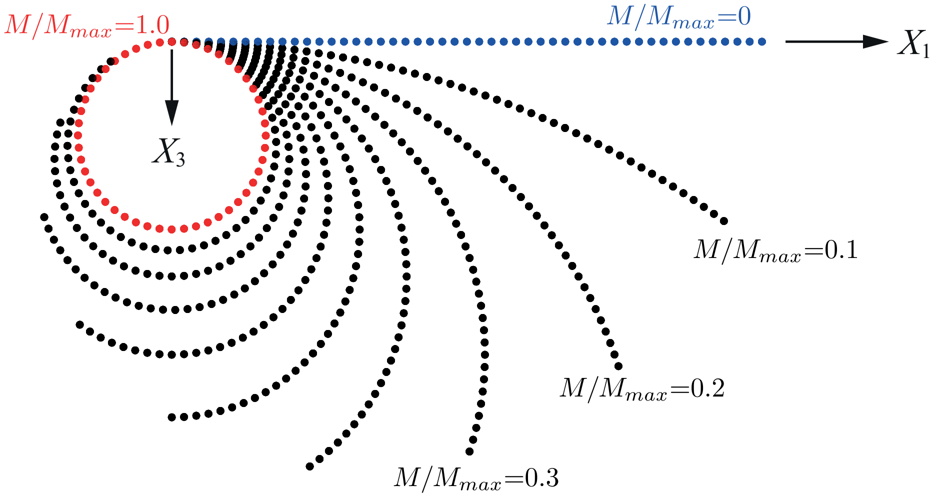

Figure 13: Deformed shapes of rectangular cantilever plate for different M/M_{max} values.

For the proposed method with the finite rotation formulation, the deformed shapes of the rectangular cantilever plate are obtained and illustrated for different M/M_{max} values with the uniform increments, 0.1 in Fig. 13. Initial configuration is illustrated by the blue color while the deformed shape at the last load step is plotted in red.

5.3. Roll up of a trapezoidal plate

The third numerical example is adopted from Başar and Ding [6]. The loading and BCs are same as the previous numerical example, tip moment is applied keeping the other end clamped. The problem is schematically illustrated in Fig. 14(a). The tip moment is incrementally applied up to load factor, λ=1.5.

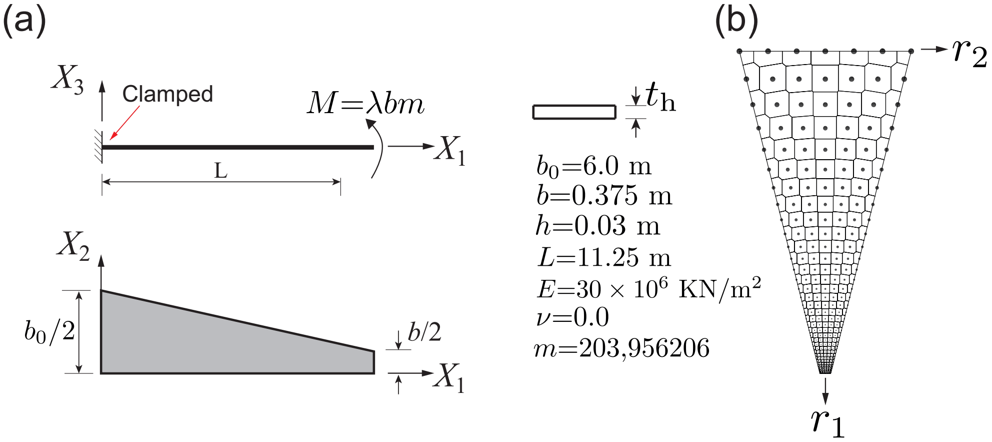

Figure 14: Modeling of cantilever trapezoidal plate: (a) representative model and main properties, (b) meshfree model with Voronoi cells.

The nodal distance of the trapezoidal model is gradually varied as shown in Fig. 14(b). This problem is also a specific finite rotation problem and without finite rotation formulation, the maximum load factor cannot be reached. At first, the results obtained by the proposed method with finite rotation formulation are compared with the FEM based results as well as reference results obtained by digitizing the graphical data of Ref. [6].

It is evident from Fig. 15 that the proposed method with finite rotation formulation agrees well with the reference and FEM results. The tip rotation given by Ref. [6] is 540°, while the tip rotation evaluated by the present method considering finite rotation is 538.7° and the error percentage becomes 0.249 %.

When the finite rotation formulation is not taken into account, the maximum load factor cannot be reached, the solution fails to converge and stops

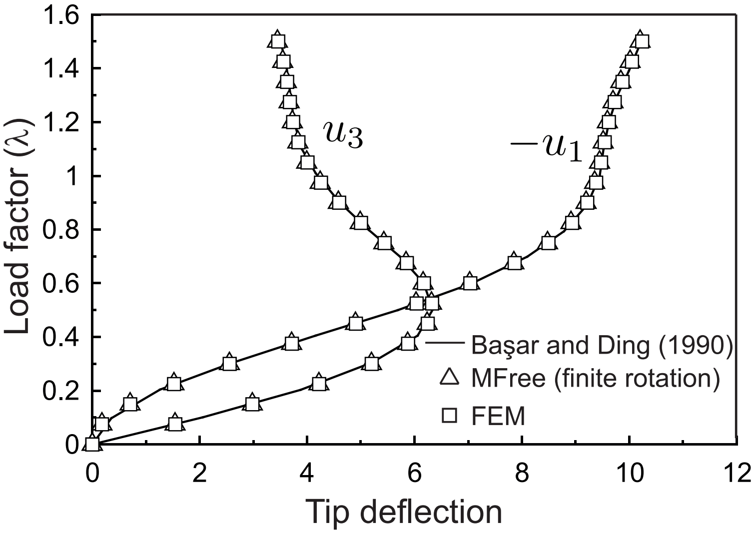

Figure 15: Comparison of meshfree results with those of FEM and Ref. [6].

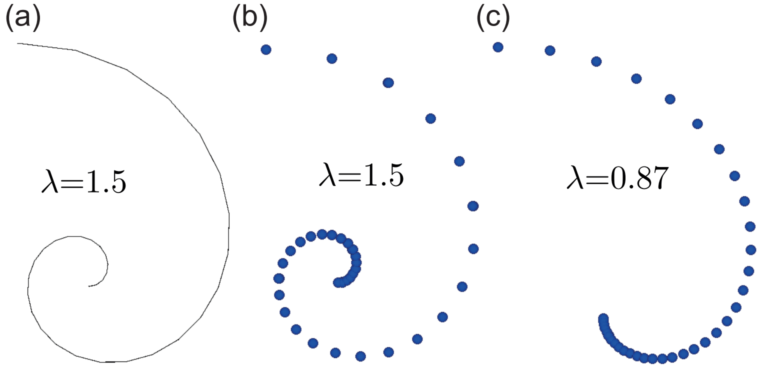

Figure 16: Deformed shapes for trapezoidal plate: (a) FEM, (b) MFree (finite rotation), (c) MFree (without finite rotation).

at λ=0.87. At this time, the number of convergence iterations is 88 for this load increment and average number of the convergence iterations becomes 41.3 for each load increment. On the other hand, average number of the convergence iterations is 3.3 when the finite rotation formulation is utilized. It is apparent that the finite rotation formulation not only improves the accuracy of the solutions but also the computational efficiency for the large rotation problems.

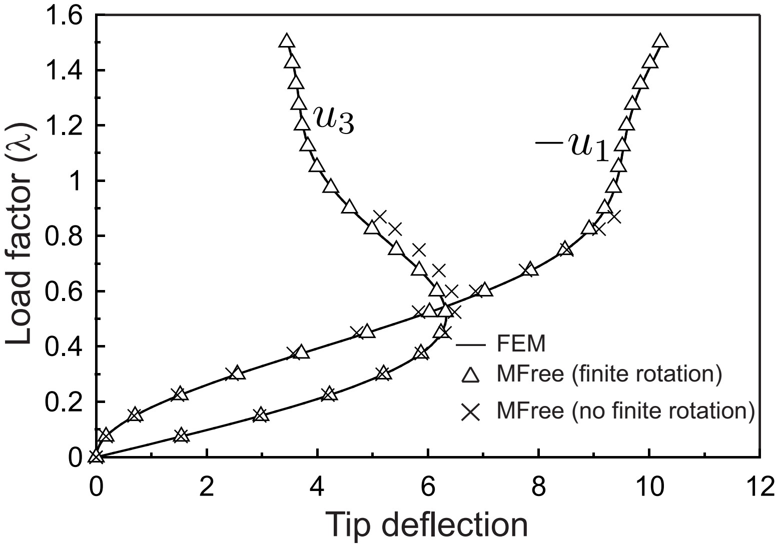

Figure 17: Influence of finite rotation formulation on the tip displacements of the trapezoidal plate.

The results obtained for with and without finite rotation formulation are compared with those of FEM. The results given in Fig. 17 shed light on the influence of finite rotation formulation on the accuracy of the numerical simulations. The displacements are slightly overestimated when the finite rotation formulation is not considered. This could be because of the work done by the external loads is mainly compensated by the displacements but not by the rotations due to the small rotation increment assumption. The deformed shapes obtained by the proposed method employing finite rotation formulation for different λ values are given in Fig. 18. The deformed shapes are illustrated for the uniform λ increments of 0.15. The initial configuration is depicted in blue color, while the deformed shape at the last load step is represented in red color.

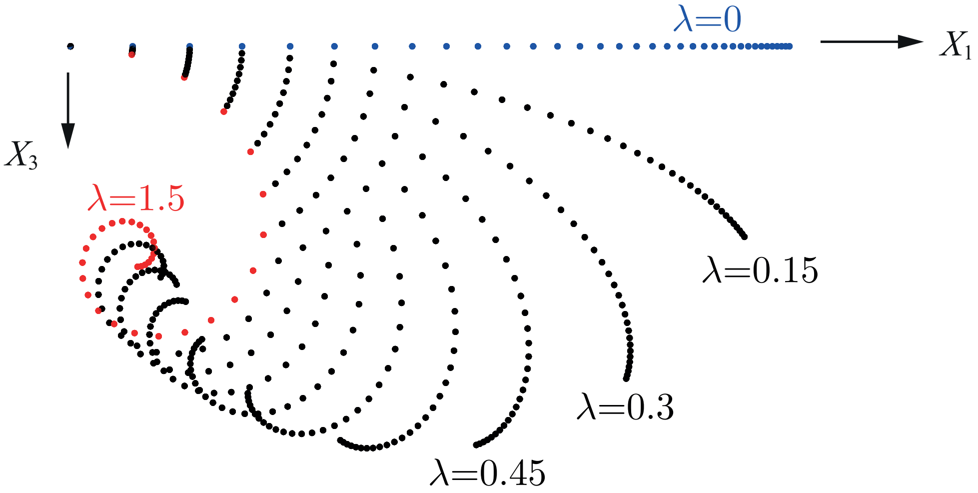

Figure 18: Deformed shapes of trapezoidal cantilever plate for different λ values.

5.4. Roll up of an L-shaped plate

The final numerical example is the roll up of an L-shaped plate. This model was examined by Ref. [60] but only deformed shapes were given, the numerical results were neither plotted nor tabulated in [60]. The main dimensions and the material properties are adopted as same as given by [60]. L-shaped plate is schematically illustrated in Fig. 19. The main dimensions are L=12, B=3 and the thickness is t_h=0.03. The elastic modulus and the Poisson's ratio are respectively adopted as E=3 × 10^7, ν=0.0. One edge of the L-shaped plate is assumed to be clamped as shown in Fig. 19, tip moment is applied to free edge, whose magnitude is defined as m=λm_ref. Here, m_ref=100 is utilized.

The L-shaped plate problem has a strongly nonlinear behavior and relatively fine mesh is necessary to accurately capture the displacements and rotations. In the meshfree models, nodal division is therefore considered as $B/15$. As opposed to previous numerical examples, this model is an assembly of two plates. In this case, a special numerical integration technique, SSCI [24-27] is implemented along connecting edges for efficient smoothing

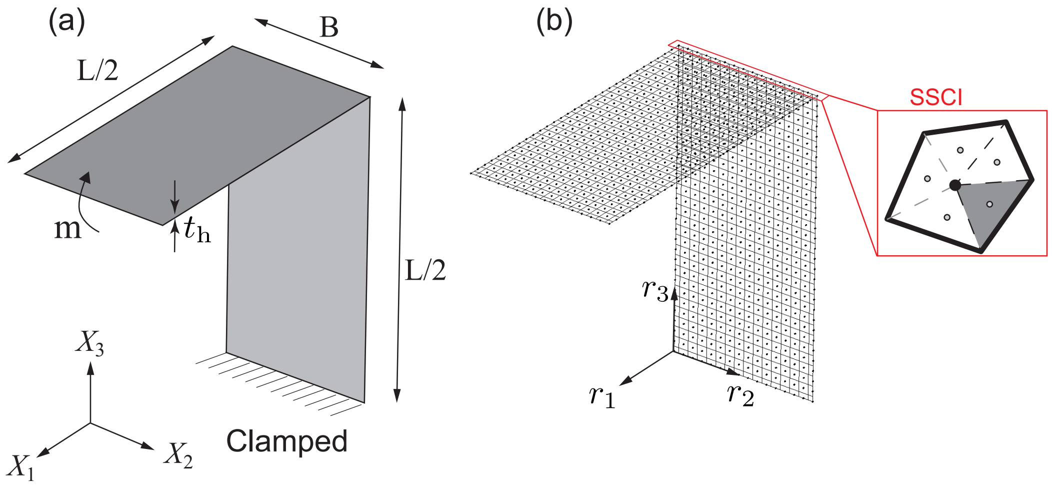

Figure 19: Modeling of L-shaped plate: (a) representative model and main dimensions, (b) meshfree model with Voronoi cells and SSCI.

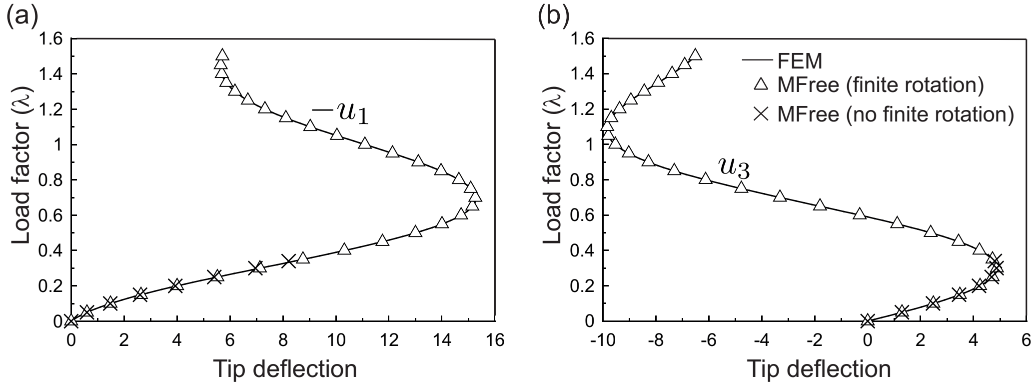

Figure 20: Comparison of tip displacements obtained by present formulation and FEM: (a) horizontal displacements,$-u_1$, (b) vertical displacements, u_3.

of physical values along the connection. In the SSCI approximation, the integration domains for SCNI are further divided into triangular sub-domains as shown in Fig. 19(b).

Assembly process for flat and curved shells has been respectively studied by the authors in Refs. [45,46]. Same assembly procedure with our previous studies is employed here.

As pointed out before, the numerical results were not provided by [60], we then conduct FEM simulations for the comparison. The tip displacements obtained by FEM and present method are compared in Fig. 20. When the finite rotation formulation is utilized, the meshfree results perfectly coincide with those evaluated by FEM. This agreement can also be spotted by the deformed shapes at the end of loading given in Fig. 21(a) and (b). On the other hand, for without finite rotation case, the solution fails to convergence and the simulation stops at λ=0.34. The deformed shape for this λ value is given in Fig. 21(c). When a detailed look is given to Fig. 20(b), it is seen that the proposed method without finite rotation formulation fails to convergence at the first turning point for vertical displacements. Beyond this point, the behavior of the L-shaped plate becomes more complicated and it can be pointed that it is difficult to trace such a complicated behavior without finite rotation formulation.

The tip rotation value at the end of loading obtained by FEM is 509.3°, while the rotation becomes 509.1° for the meshfree computations. The difference between the results is 0.046 %. The average number of convergence iterations for each load increment is 4.3 in case of the finite rotation formulation is introduced. On the other hand, that value becomes 15.7 for without finite rotation formulation. As it is pointed out above, the solution stops at λ=0.34. Compared to other numerical examples, the solution stops at the lowest load level in case of L-shaped problem for without finite rotation formulation, which clearly indicates the strongly nonlinear behavior of the problem. Moreover, even if the finite rotation formulation is considered, the average number of convergence iterations for each load increment is 4.3. This value is larger than those of other problems examined so far, which are 2.1, 2.2 and 3.3 for pinched cylinder, rectangular plate and trapezoidal plate cases, respectively. For the last numerical example, the L-shaped plate, the deformed shapes are portrayed for different λ values with uniform increments of 0.1 in Fig. 22. The figure indicates that the deformation is highly nonlinear and the rotation increments are large.

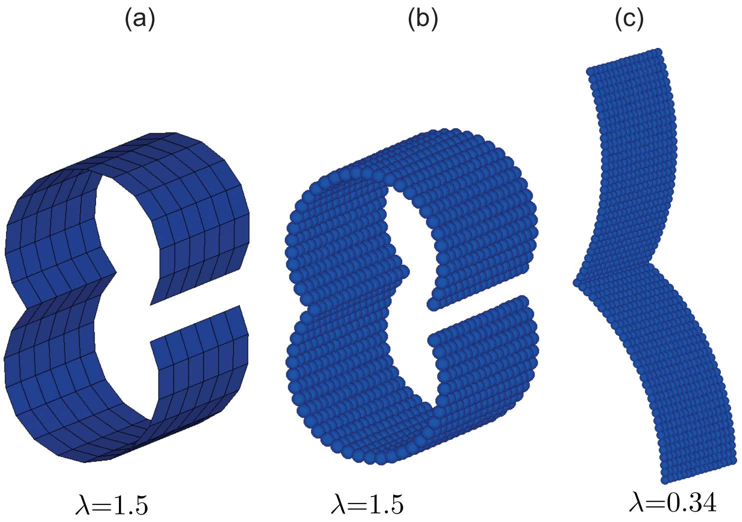

Figure 21: Deformed shapes obtained at the last load steps by (a) FEM, (b) MFree (finite rotation), (c) MFree (without finite rotation).

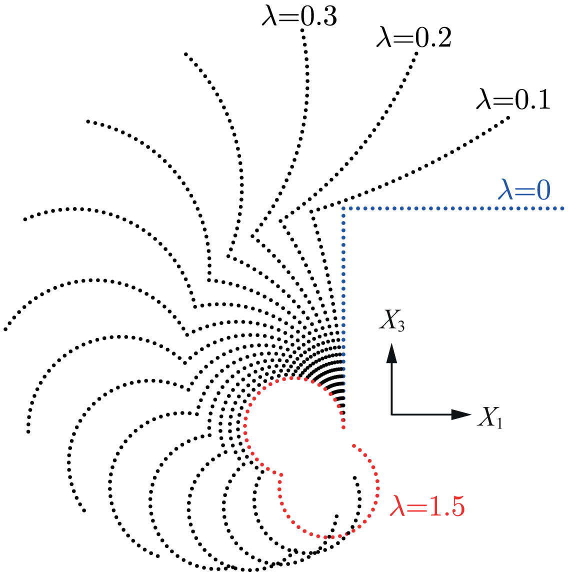

Figure 22: Deformed shapes of L-shaped plate for different λ values.

6. Conclusions

In this contribution, we have presented an enhanced meshfree formulation considering finite rotations for geometrically nonlinear analysis of flat, curved, and folded shells. The results obtained by the proposed method with and without finite rotation formulation were compared with available reference results and FEM based solutions obtained by the authors. The results, when the finite rotation formulation is considered, apparently showed very good agreement with the reference results. In contrast, the formulation without considering finite rotation is not able to capture the nonlinearity of the present numerical examples. Furthermore, the computational efficiency was improved by introducing finite rotation even for the pinched cylinder case, which is not a specific finite rotation problem. As for the specific finite rotation problems, the finite rotation formulation significantly improved both the solution accuracy and the computational efficiency. In case of the without finite rotation solutions, the solutions failed to converge and the solutions stopped before reaching the maximum load level.

Acknowledgments

The authors are grateful to Mr. Kohei Nishiguchi (Graduate School of Engineering, Hiroshima University) for the valuable support and discussions.

References

[1] J.L. Sanders Jr., Nonlinear theories for thin shells, Q. Appl. Math. 21(1963)21-36.

[2] A. Libai, J.G. Simmonds, Highly non-linear cylindrical deformations of rings and shells, Int. J. Non-Linear Mech. 18(1983)181-197.

[3] H. Stumpf, On the non-linear buckling and post-buckling analysis of thin elastic shells, Int. J. Non-Linear Mech. 19(1984)195-215.

[4] E. N. Dvorkin, K. Bathe, A continuum mechanics based four-node shell element for general non-linear analysis, Eng. Computation 1(1984)77-88.

[5] N. Stander, A. Matzenmiller, E. Ramn, An assessment of assumed strain methods in finite rotation shell analysis, Eng. Computation 6(1989)58-66.

[6] Y. Başar, Y. Ding, Finite-rotation elements for the non-linear analysis of thin shell structures, Int. J. Solid Struct. 26(1990)83-97.

[7] Y. Başar, Y. Ding, W.B. Krätzig, Finite-rotation shell elements via mixed formulation, Comput. Mech. 10(1992)289-306.

[8] Y. Başar, Y. Ding, R. Shultz, Refined shear-deformation models for composite laminates with finite rotations, Int. J. Solid Struct. 30(1993)2611-2638.

[9] Y. Başar, U. Montag, Y. Ding, On an isoparametric finite-element for composite laminates with finite rotations, Comput. Mech. 12(1993)329-348.

[10] M. Amabili, Non-linearities in rotation and thickness deformation in a new third-order thickness deformation theory for static and dynamic analysis of isotropic and laminated doubly curved shells, Int. J. Non-Linear Mech. 69(2015)109-128.

[11] M. Amabili, A new third-order shear deformation theory with non-linearities in shear for static and dynamic analysis of laminated doubly curved shells, Compos. Struct. 128(2015)260-273.

[12] M.G. Rivera, J.N. Reddy, M. Amabili, A new twelve-parameter spectral/hp shell finite element for large deformation analysis of composite shells, Compos. Struct. 151(2016)183-196.

[13] M. Amabili, Nonlinear Mechanics of Shells and Plates: Composite, Soft and Biological Materials, Cambridge University Press, New York, USA, 2018.

[14] M.G. Rivera, J.N. Reddy, M. Amabili, A continuum eight-parameter shell finite element for large deformation analysis, Mech. Adv. Mater. Struc. 2019, https://doi.org/10.1080/15376494.2018.1484531.

[15] W.K. Liu, S. Jun, Y.F. Zhang, Reproducing kernel particle methods, Int. J. Numer. Meth. Fluid. 20(1995)1081-1106.

[16] S. Jun, W.K. Liu, T. Belytschko, Explicit reproducing kernel particle methods for large deformation problems, Int. J. Numer. Meth. Eng. 41(1998)137-166.

[17] W.K. Liu, S. Jun, Multiple-scale reproducing kernel particle methods for large deformation problems, Int. J. Numer. Meth. Eng. 41(1998)1339-1362.

[18] S. Li, W. Hao, W.K. Liu, Numerical simulations of large deformation of thin shell structures using meshfree methods, Comput. Mech. 25(2000)102-116.

[19] K.M. Liew, T.Y. Ng, Y.C. Wu, Meshfree method for large deformation analysis - a reproducing kernel particle approach, Eng. Struct. 24(2002)543-551.

[20] K.M. Liew, L.X. Peng, S. Kitipornchai, Nonlinear analysis of corrugated plates using a FSDT and a meshfree method, Comput. Meth. Appl. Mech. Eng. 196(2007)2358-2376.

[21] X. Zhao, Y. Yang, K.M. Liew, Geometrically nonlinear analysis of cylindrical shells using the element-free kp-Ritz method, Eng. Anal. Bound. Elem. 31(2007)783-792.

[22] J.S. Chen, C.T. Wu, S. Yoon, Y. You, A stabilized conforming nodal integration for Galerkin mesh-free methods, Int. J. Numer. Meth. Eng. 50(2001)435-466.

[23] J.S. Chen, S. Yoon, C.T. Wu, Non-linear version of stabilized conforming nodal integration for Galerkin mesh-free methods, Int. J. Numer. Meth. Eng. 53(2002)2587-2615.

[24] D. Wang, J.S. Chen, A Hermite reproducing kernel approximation for thin-plate analysis with sub-domain stabilized conforming integration, Int. J. Numer. Meth. Eng. 74(2008)368-390.

[25] D. Wang, H. Peng, A Hermite reproducing kernel Galerkin meshfree approach for buckling analysis of thin plates, Comput. Mech. 51(2013)1013-1029.

[26] D. Wang, C. Song, H. Peng, A circumferentially enhanced Hermite reproducing kernel meshfree method for buckling analysis of Kirchhoff-Love cylindrical shells, Int. J. Struct. Stabil. Dynam. 15(2015)1450090.

[27] D. Wang, J. Wu, An efficient nesting sub-domain gradient smoothing integration algorithm with quadratic exactness for Galerkin meshfree methods, Comput. Meth. Appl. Mech. Eng. 298(2016)485-519.

[28] D. Wang, J. Wu, An inherently consistent reproducing kernel gradient smoothing framework toward efficient Galerkin meshfree formulation with explicit quadrature, Comput. Meth. Appl. Mech. Eng. 349(2019)628-672.

[29] D. Wang, Y. Sun, A Galerkin meshfree method with stabilized conforming nodal integration for geometrically nonlinear analysis of shear deformable plates, Int. J. Comput. Methods 8(2011)685-703.

[30] D. Wang, Y. Sun, An efficient Galerkin meshfree formulation for shear deformable beam under finite deformation, Theor. Appl. Mech. Lett. 1(2011)051010.

[31] Y.X. Peng, A.M. Zhang, F.R. Ming, A thick shell model based on reproducing kernel particle method and its application in geometrically nonlinear analysis, Comput. Mech. 62(2018)309-321.

[32] S. Tanaka, S. Sadamoto, S. Okazawa, Large deflection analysis for thin plates using the Hermite reproducing kernel (HRK) approximation, Theor. Appl. Mech. Jpn. 60(2012)205-214.

[33] S. Tanaka, S. Sadamoto, S. Okazawa, Nonlinear thin-plate bending analyses using the Hermite reproducing kernel approximation, Int. J. Comput. Methods 9(2012)1240012.

[34] S. Sadamoto, S. Tanaka, S. Okazawa, Elastic large deflection analysis of plates subjected to uniaxial thrust using meshfree Mindlin-Reissner formulation, Comput. Mech. 52(2013)1313-1330.

[35] S. Sadamoto, S. Tanaka, S. Okazawa, Buckling analysis of plate with an initial imperfection using RKPM based on convected coordinate system, J. Jpn. Soc. Naval Arch. Ocean Eng. 19(2014)169-178 (in Japanese).

[36] S. Sadamoto, S. Tanaka, S. Okazawa, Modeling of plate structures for Galerkin meshfree methods (2nd report: Geometrical non-linear analysis), Trans. Jpn. Soc. Mech. Eng. 81(2015)15-00252 (in Japanese).

[37] J.S. Chen, H.P. Wang, New boundary condition treatments in meshfree computation of contact problems, Comput. Meth. Appl. Mech. Eng. 187(2000)441-468.

[38] W. Li, N. Nguyen-Thanh, K. Zhou, Geometrically nonlinear analysis of thin-shell structures based on an isogeometric-meshfree coupling approach, Comput. Meth. Appl. Mech. Eng. 336(2018)111-134.

[39] H. Noguchi, T. Kawashima, T. Miyamura, Element free analyses of shell and spatial structures, Int. J. Numer. Meth. Eng. 47(2000)1215-1240.

[40] D. Wang, J.S. Chen, Locking-free stabilized conforming nodal integration for meshfree Mindlin-Reissner plate formulation, Comput. Meth. Appl. Mech. Eng. 193(2004)1065-1083.

[41] D. Wang, J.S. Chen, A locking-free meshfree curved beam formulation with the stabilized conforming nodal integration, Comput. Mech. 39(2006)83-90.

[42] S. Tanaka, H. Suzuki, S. Sadamoto, M. Imachi, T.Q. Bui, Analysis of cracked shear deformable plates by an effective meshfree plate formulation, Eng. Fract. Mech. 144(2015)142-157.

[43] S. Tanaka, H. Suzuki, S. Sadamoto, S. Okazawa, T.T. Yu, T.Q. Bui, Accurate evaluation of mixed-mode intensity factors of cracked shear-deformable plates by an enriched meshfree Galerkin formulation, Arch. Appl. Mech. 87(2017)279-298.

[44] S. Sadamoto, M. Ozdemir, S. Tanaka, K. Taniguchi, T.T. Yu, T.Q. Bui, An effective meshfree reproducing kernel method for buckling analysis of cylindrical shells with and without cutouts, Comput. Mech. 59(2017)919-932.

[45] S. Sadamoto, S. Tanaka, K. Taniguchi, M. Ozdemir, T.Q. Bui, C. Murakami, D. Yanagihara. Buckling analysis of stiffened plate structures by an improved meshfree flat shell formulation. Thin-Walled Struct. 117(2017)303-313.

[46] M. Ozdemir, S. Sadamoto, S. Tanaka, S. Okazawa, T.T. Yu, T.Q. Bui, Application of 6-DOFs meshfree modeling to linear buckling analysis

of stiffened plates with curvilinear surfaces, Acta Mech. 229(2018)4995-5012.

[47] S. Tanaka, M.J. Dai, S. Sadamoto, T.T. Yu, T.Q. Bui, Stress resultant intensity factors evaluation of cracked folded structures by 6DOFs flat shell meshfree modeling, Thin-Walled Struct. 144(2019)106285.

[48] W. Kanok-Nukulchai, A simple and efficient finite element for general shell analysis, Int. J. Numer. Meth. Eng. 14(1979)179-200.

[49] K.S. Surana, Geometrically nonlinear formulation for the curved shell elements, Int. J. Numer. Meth. Eng. 19(1983)581-615.

[50] H. Noguchi, T. Hisada, An efficient formulation for a shell element considering finite rotation increments and its assessment, Trans. Jpn. Soc. Mech. Eng. 58(1992)943-950 (in Japanese).

[51] H. Parisch, An investigation of a finite rotation four node assumed strain shell element, Int. J. Numer. Meth. Eng. 31(1991)127-150.

[52] J. Argyris, An excursion into large rotations, Comput. Meth. Appl. Mech. Eng. 32(1982)85-155.

[53] H. Noguchi, T. Hisada, Sensitivity analysis in post-buckling problems of shell structures, Comput. Struct. 47(1993)699-710.

[54] T. Hisada, H. Noguchi, Basic and application of nonlinear finite element method, (1995) Maruzen (in Japanese).

[55] S. Sadamoto, Nonlinear analyses of folded-plate structure using meshfree method, Doctoral dissertation, Graduate School of Engineering, Hiroshima University, 2014 (in Japanese).

[56] ANSYS vers. 17.2(2016)

[57] R.A.F. Valente, R.M.N. Jorge, R.P.R. Cardoso, J.M.A. César de Sá, J.J.A. Grácio, On the use of an enhanced transverse shear strain shell element for problems involving large rotations, Comput. Mech. 30(2003)286-296.

[58] K.Y. Sze, X.H. Liu, S.H. Lo, Popular benchmark problems for geometric nonlinear analysis of shells, Finite Elem. Anal. Des. 40(2004)1551-1569.

[59] J. Chróścielewski, W. Witkowski, Four-node semi-EAS element in six-field nonlinear theory of shells, Int. J. Numer. Meth. Eng. 68(2006)1137-1179.

[60] J. Chróścielewski, J. Makowski, H. Stumpf, Finite element analysis of smooth, folded and multi-shell structures, Comput. Meth. Appl. Mech. Eng. 141(1997)1-46.